UC San Diego
UC San Diego Previously Published Works

Title

ADCP-based estimates of lateral turbulent Reynolds stresses in wavy coastal environments

Permalink

Journal

ISSN

Authors

Amador, Andre
Giddings, Sarah N
Pawlak, Geno

Publication Date

DOI

Peer reviewed

ADCP-based estimates of lateral turbulent Reynolds stresses in wavy coastal environments

Andre Amador [1,2], Sarah N. Giddings [2], Geno Pawlak [1,2]*

[1]Mechanical and Aerospace Engineering, University of California San Diego, La Jolla, California
[2]Scripps Institution of Oceanography, University of California San Diego, La Jolla, California

Abstract

We assess the use of a four-beam, Janus-type ADCP for the measurement of lateral Reynolds stress ($\overline{u'v'}$) in wavy coastal environments. The calculation of $\overline{u'v'}$ derives either from the fluctuating beam velocity equations or directly from the fluctuating part of the Cartesian velocities (u', v'), with each requiring different assumptions. We adapt existing wave-turbulence decomposition strategies to isolate the lateral turbulent motions at frequencies below those of surface gravity waves. The performance of the proposed method is evaluated via comparisons with independent ADV-based stress estimates at two sites. Comparisons show good quantitative agreement over the tidal cycle, and indicate that ADCPs can effectively resolve lateral turbulent fluxes via ensemble-averaging. Assessment of ensemble-averaged turbulence cospectra indicates that the proposed approach is effective in isolating the low-frequency (below the waveband) turbulent stresses from wave-induced errors. Furthermore, the vertical structure of the turbulent Reynolds stresses is examined as a function of tidal phase in an unstratified, tidally-driven flow over a rough coral reef seabed in weak swell conditions. Observations and analysis indicate that lateral fluxes are tied to the cross-shore (lateral) gradient of the mean alongshore flow, though vertical and lateral stresses are primarily driven by bottom-generated turbulence. Scaling considerations indicate that cross-shore transport by lateral turbulent mixing could be relevant to coral reef shelves with steep cross-reef slopes and rough bottoms.

Turbulence plays a key role in the transport of momentum, mass and heat, and affects a range of coastal processes including oceanic bottom boundary layer dynamics (Trowbridge and Lentz 2018), wave dissipation, and nearshore circulation (Brink 2016). Accurate estimation of Reynolds stresses is therefore critical for quantifying coastal ocean dynamics and mixing. Enhanced mixing of nutrients due to turbulent processes also contributes to the health of the coral reef benthic community (Baird and Atkinson 1997; Atkinson et al. 2001; Monismith 2007; Davis et al. 2021), to the dispersal and distributions of biological material (Jones et al. 2009; Sevadjian et al. 2010), and has important implications for nearshore water quality.

Vertical profiles of Reynolds stresses can be obtained from ADCPs using the variance method (Lohrmann et al. 1990; Stacey et al. 1999a) which makes use of the difference of along-beam velocity variances. In the coastal ocean, however, the effects of surface gravity waves complicate the measurement of the turbulent stresses. This is because the oscillating wave velocities are typically orders of magnitude larger than the turbulent fluctuations, and often occur in the same frequency band as the stress-carrying turbulent motions (Trowbridge 1998; Trowbridge and Elgar 2001; Kirincich and Rosman 2011). Thus, small uncertainties in sensor tilt or the effects of a sloping bottom can introduce velocity correlations that dominate the covariance spectrum, potentially biasing the Reynolds stress estimates (Trowbridge 1998). Unsteady advection by wave orbital motions can also modify the observed frequency cospectrum by aliasing lower frequency turbulent energy into the waveband (Lumley and Terray 1983; Gerbi et al. 2008; Rosman and Gerbi 2017; Trowbridge et al. 2018). This leads to an apparent decrease in the observed spectral density in frequencies below the waveband, and also results in biased stress estimates.

A variety of wave-turbulence decomposition techniques have been proposed to estimate turbulent fluxes in the presence of waves (e.g., Trowbridge 1998; Shaw and Trowbridge 2001; Bricker and Monismith 2007; Feddersen and Williams 2007; Gerbi et al. 2008; Bian et al. 2018). For instance, velocity differencing (e.g., Trowbridge 1998) and adaptive filtering (e.g., Shaw and Trowbridge 2001; Rosman et al. 2008)

---

*Correspondence: pawlak@ucsd.edu

Additional Supporting Information may be found in the online version of this article.

strategies use adjacent velocity measurements to remove wave biases from the Reynolds stress signal. These methods assume that wave velocities are correlated or coherent over spatial scales that are much larger than those associated with turbulent fluctuations; hence, motions that correlate between the measurements are assumed to be due to waves, while motions that do not correlate are attributed to turbulence. On the other hand, cospectra-fit (CF) methods (e.g., Gerbi et al. 2008; Kirincich et al. 2010) fit a semi-empirical model of boundary layer turbulence derived by Kaimal et al. (1972) to the observed cospectrum at frequencies smaller than those of surface gravity waves to estimate the turbulent stresses. While originally developed for acoustic Doppler velocimeters (ADVs), these techniques have been successfully adapted for ADCP measurements (e.g., Whipple et al. 2006; Rosman et al. 2008; Kirincich et al. 2010); thus, extending the applicability of the variance method to enable vertical Reynolds stress estimates in wavy environments.

Research on wave-bias removal from turbulence estimates has been mostly limited to observations of vertical momentum fluxes ($\overline{u'w'}$ and $\overline{v'w'}$). In contrast, there has been little discussion about the turbulence statistics associated with the lateral momentum fluxes ($\overline{u'v'}$) in the nearshore and inner-shelf literature. For coastal flows, it is generally assumed that the horizontal length scales are much larger than the vertical length scales (Burchard 2002; Burchard et al. 2008); thus, the horizontal gradients of the turbulent fluxes are often neglected. As a result, lateral mixing processes may not be represented accurately in fine-scale coastal ocean models and are unlikely to be resolved in larger scale models. Coastal boundaries require further attention as spatial gradients in bottom roughness and water depth (bottom drag) can lead to substantial cross-shore shear in the alongshore flow, and hence to enhanced turbulent mixing and lateral transport (Brink 2016). At present, direct measurements of inner-shelf turbulence are scarce, and the role of the lateral turbulent stresses in cross-shelf transport is not well understood.

The work presented here aims to offer new insights into the temporal variability and vertical structure of the Reynolds stresses in tidally-dominated coral reef environments. In this paper, we evaluate the use of a four-beam, Janus-type ADCP to estimate lateral Reynolds stresses in the presence of surface gravity waves. The method uses a variation of Kirincich et al.'s (2010) procedure for isolating the turbulent motions at frequencies lower than those of surface waves. The performance is assessed by comparing the ADCP-based Reynolds stress estimates with ADV-based estimates. The experimental data used in this study were collected at the Makua reef on the western coast of O'ahu, Hawai'i (Fig. 1) in tidally-driven, unstratified flow under weak swell conditions.

The work here is presented as follows. The observations and methods are introduced in the next section (*Materials and procedures*) including a detailed description of the proposed ADCP-based stress calculation method. In Results, we take an ensemble-averaged view of the turbulent properties of the flow. The phase ensemble-averaging procedure is described first (Phase ensemble averaging), followed by an inspection of ensemble-averaged turbulent cospectra (Section: *Turbulence cospectra and roll-off wavenumbers*) and of the associated turbulent length scales (Section: *Turbulence length scales*). We then evaluate the performance of the proposed method by comparing results with ADV measurements, and characterize the vertical structure of the turbulent Reynolds stresses as a function of tidal phase (Section: *Reynolds stress estimates*). Three simple eddy viscosity models for the lateral Reynolds stress component are proposed and tested (Section: *Model for lateral Reynolds stress*). Potential limitations of the proposed method and implications for cross-shore turbulent transport are discussed in *Implications of the results*.

Materials and procedures

Field deployment

Field observations were carried out offshore of Makua (21.510°, −158.236°) on the west coast of O'ahu, Hawai'i (Fig. 1) in September 2013. The study specifically targeted the resolution of hydrodynamics over the forereef region in varying wave and current conditions. Field data from fixed instrumentation were collected as described in Arzeno et al. (2018) (*see* also Amador et al. 2020). A brief summary of the field experiment is presented next.

Isobaths at the Makua forereef are oriented roughly north–south and aligned with the coastline. Bathymetry features a low slope region extending to about 600 m from the shoreline with an average depth of 6 m, followed by a fairly constant cross-shore seafloor slope of about 3.5% between the 6- and 24-m isobaths; beyond this limit, the coral reef shelf drops off sharply in the offshore direction. The Makua forereef exhibits intermittent, shore-normal spur, and groove formations between the 6- and 16-m isobaths. The bottom substrate is primarily composed of rough reef interspersed with pockets of sandy coral rubble and scattered patches of coral colonies.

Two 1200-kHz Teledyne RD Instruments (RDI) Workhorse ADCPs were deployed on rigid frames near the 12 m isobath (Fig. 1) to resolve velocity fluctuations associated with the forereef turbulent flow. These bottom-mounted ADCPs (hereafter referred to as 12N and 12S) were moored about 260 m apart, and configured to sample in 0.25-m bins with a blanking distance of 0.8 m and a sampling frequency of 0.5 Hz using water sampling mode 12 (fast ping mode). Both 12N and 12S y (3–4 beam) axes were nearly aligned with the principal axis of the depth-averaged flow (Table 1). A third 300-kHz ADCP (hereafter referred to as 20W) was deployed roughly 270 m offshore of 12N near the 20 m isobath (Fig. 1), and was configured to sample water velocities at 0.5 Hz in 1.25-m bins with a blanking distance of 3.25 m. ADCPs were programmed to record pressure at the bed and raw velocities in beam coordinates continuously. Thermistor chains (T-chains) located near
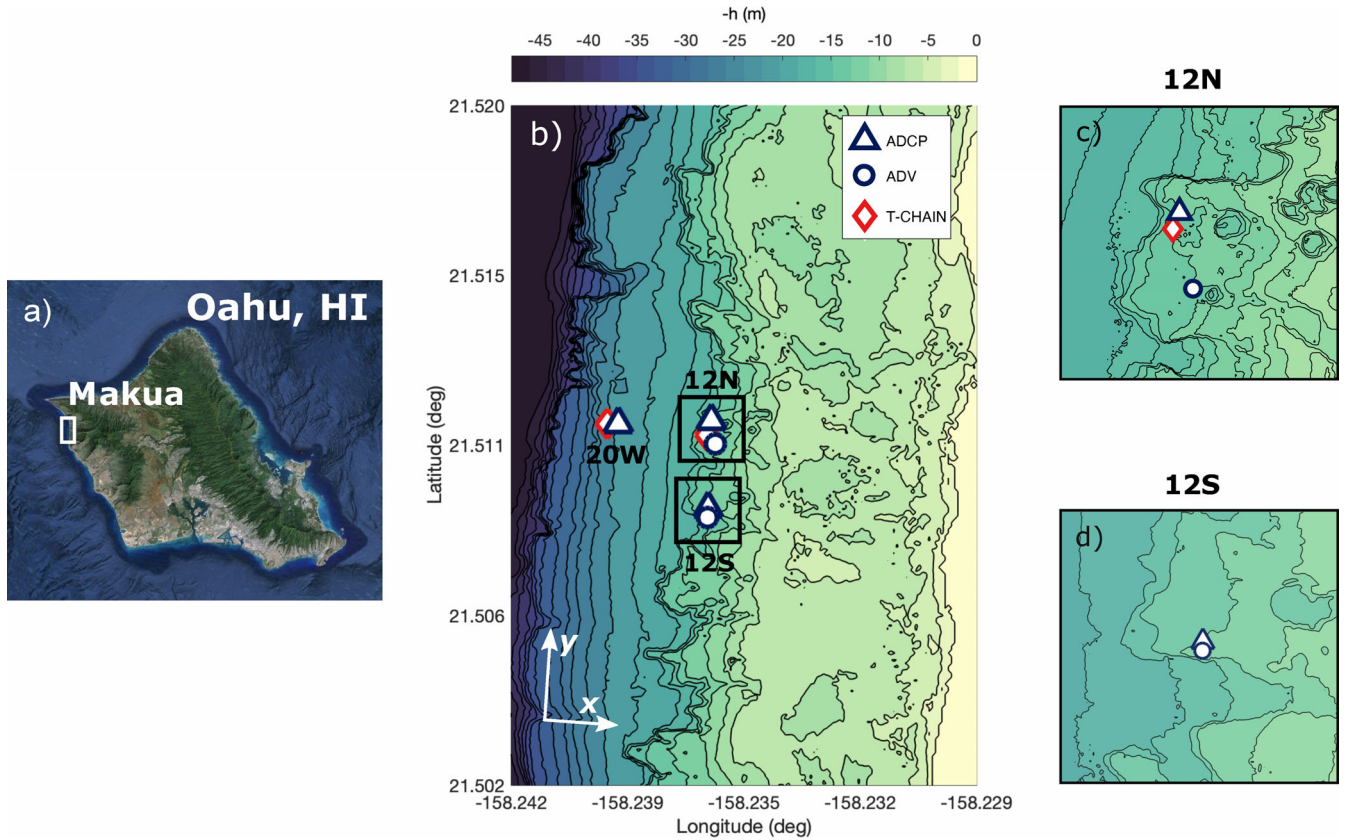
Fig. 1. (**a**) Satellite image (Google Earth) of Oʻahu, Hawaiʻi, (**b**) Makua study site and instrument array with LIDAR bathymetry, (**c**) 12N mooring, and (**d**) 12S mooring. The notations 12N, 12S, and 20W denote the location (i.e., north, south, west) of the observational array near the 12- and 20-m isobaths. The coordinate system (x, y) defines the cross- and alongshore directions, respectively, and is roughly aligned with the principal axis of the flow (defined locally at each site).

the 12N and 20W ADCPs (Fig. 1) measured temperature at 2 Hz from 0.30 m above the bed to 1 m below the surface in 1- and 2-m intervals, respectively. Table 1 provides additional details about the ADCP array setup.

Three 6-MHz Nortek Vector acoustic Doppler velocimeters (ADVs) were deployed on a 3-m vertical spar located 70 m south of ADCP 12N (Fig. 1). The ADVs were configured to sample at 16 Hz in 16-min bursts every hour. The upper-most probe was oriented upward with a sampling volume located 3 m above the bed (m.a.b); two downward-looking probes sampled water velocities 1.5 m.a.b with a horizontal separation distance of 1 m. An additional upward-looking 6-MHz Nortek Vector ADV was mounted on a vertical bar collocated with ADCP 12S (Fig. 1). The latter was configured to sample ∼ 1.4 m above the bed at 16 Hz in hourly bursts of 12 min.

The observational period featured weak swell conditions (Fig. 2a) with minimal short-period wave energy (Fig. 2b), and generally light winds (not shown). Significant wave heights (H_{sig}) and peak periods (T_p) were calculated from ADCP pressure data using spectral analysis and linear wave theory. Tidal variations from pressure measurements at the 12N, 12S, and

20W ADCPs (Fig. 2c) show a dominant semidiurnal tidal signal, and a discernible spring-neap tidal cycle. Conditions were marked by strong semidiurnal alongshore velocities (Fig. 2d) with significantly weaker cross-shore currents (Fig. 2e). Salinity contributions to density were negligible over the observational period (Arzeno et al. 2018). Arzeno et al. (2018) estimated gradient Richardson numbers (Ri) at the 12N T-chain (not shown), and determined that conditions were unstratified ($Ri < 0.25$) 99% of the time. Time-series data of wind and water temperature difference are shown in fig. 3 in Arzeno et al. (2018).

Stress estimates from ADCP measurements

Vertical and lateral stress covariances from along-beam velocity fluctuations

The variance method (Lohrmann et al. 1990; Lu and Lueck 1999; Stacey et al. 1999a) provides direct estimates of the turbulent Reynolds stresses from the ADCP along-beam velocities. Following Stacey et al. (1999a), the along-beam (radial) velocity equations for a vertically aligned (i.e., zero tilt), upward-looking, four-beam Janus ADCP are given by

Table 1. ADCP setup.

ADCP	Mode	Depth (m)	Pitch (deg)	Roll (deg)	Orientation* (deg)
12N	12	13.2	−1.4°	−3.1°	−1.2°
12S	12	11.7	−3.6°	−2.0°	3.9°
20W	1	21.5	0.8°	−0.6°	19.4°

*Orientation of the y (3–4 beam) axis relative to the principal axis of the depth- averaged flow (positive counterclockwise).

$$b_1 = u_1\sin\theta + w_1\cos\theta$$
$$b_2 = -u_2\sin\theta + w_2\cos\theta$$
$$b_3 = v_3\sin\theta + w_3\cos\theta \qquad (1)$$
$$b_4 = -v_4\sin\theta + w_4\cos\theta$$

$$\frac{\tau_{xz}}{\rho} = -\overline{u'w'} = \frac{\overline{b_1'^2} - \overline{b_2'^2}}{4\sin\theta\,\cos\theta} \qquad (2)$$

$$\frac{\tau_{yz}}{\rho} = -\overline{v'w'} = \frac{\overline{b_3'^2} - \overline{b_4'^2}}{4\sin\theta\,\cos\theta} \qquad (3)$$

where the radial beam velocities b_i (i = 1, 2, 3, 4) are positive toward the ADCP head; u_i, v_i, and w_i are the x, y, and z velocity components at the ith beam location aligned with the ADCP reference frame; and $\theta = 20°$ is the angle of the beams away from vertical. To calculate the Reynolds stresses, the along-beam velocities are decomposed into a time-averaged mean ($\overline{b_i}$) and fluctuating (b_i') part (e.g., $b_i = \overline{b_i} + b_i'$). The vertical components of the Reynolds stress (vertical flux of horizontal momentum) are obtained by differencing the along-beam velocity variances from opposing beam pairs

where ρ is density, τ_{xz} and τ_{yz} are the vertical turbulent stress components, and the overbars indicate temporal averaging. The variance technique for the vertical stresses in Eqs. (2) and (3) requires that the turbulence statistics be stationary over the averaging interval and statistically homogeneous to second order (i.e., $\overline{u_1'^2} = \overline{u_2'^2} = \overline{u'^2}$) at the scale of the ADCP beam spread (Lu and Lueck 1999).

An expression for the lateral Reynolds stress (horizontal flux of horizontal momentum) can be derived by expanding
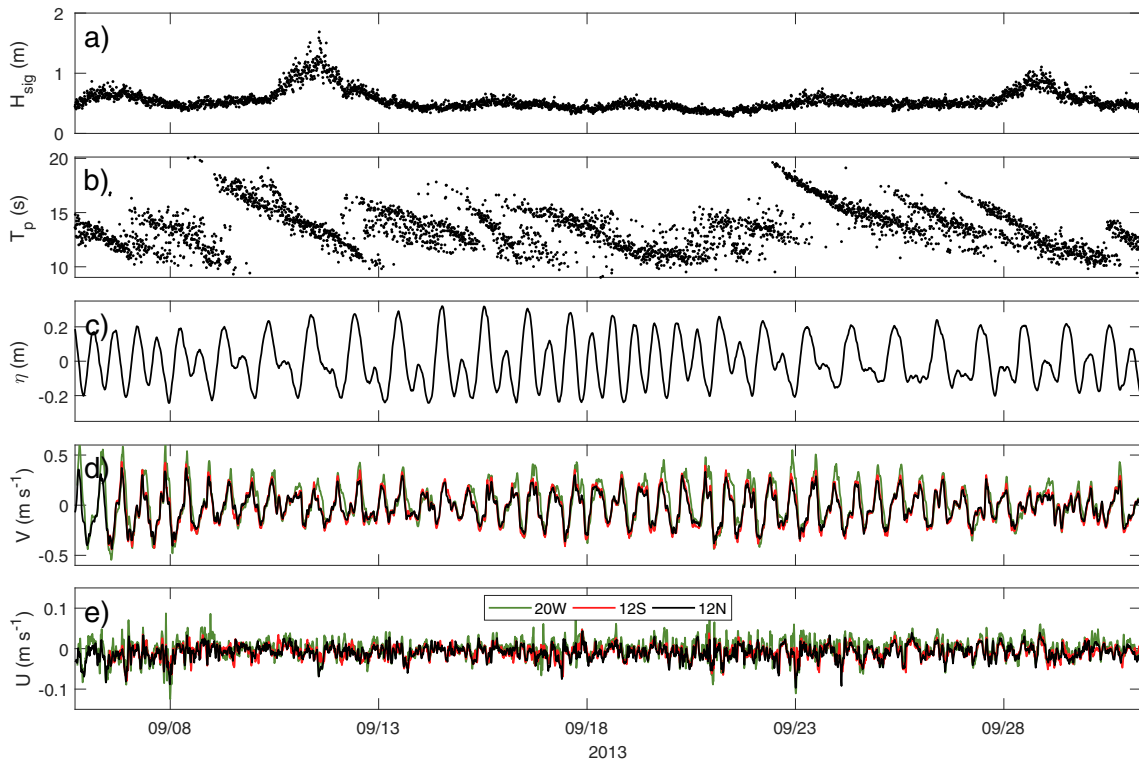

Fig. 2. Wave, sea surface height, and current conditions at the Makua fore reef based on 20-min averages with 50% overlap. The figure includes time series of (**a**) significant wave height, (**b**) peak wave period, (**c**) sea surface displacement, (**d**) depth-averaged along, and (**e**) cross-shore velocity at 12N, 12S, and 20W. Adapted from Arzeno et al. (2018).

the product $\overline{(b'_1 - b'_2)(b'_4 - b'_3)}$ and assuming spatial homogeneity (i.e., $u_1' = u_2' = u'$) across the beam field (*see* Supporting Information Section S1)

$$\frac{\tau_{xy}}{\rho} = -\overline{u'v'} = \frac{\overline{b'_1 b'_4} - \overline{b'_1 b'_3} - \overline{b'_2 b'_4} + \overline{b'_2 b'_3}}{4\sin^2\theta} \quad (4)$$

Calculation of the lateral stress using Eq. (4) is equivalent to the $\overline{u'v'}$ covariance derived from the Cartesian u' and v' velocities computed via the standard ADCP beam-to-instrument coordinate transformation. The calculation of the Cartesian velocities implicitly assumes spatial homogeneity over opposing beams. The work of Dewey and Stringer (2007), however, has shown that the assumption of spatial homogeneity can be relaxed and replaced with the assumption of uniform horizontal velocity gradients, albeit at the expense of some additional, but likely small, correction terms (*see* Supporting Information Section S1). Considering the latter assumption, a reasonable estimate of $\overline{u'v'}$ can be achieved from Eq. (4) as long as the dominant stress-carrying motions maintain a level of spatial coherence between the beams. This implies that the dominant horizontal turbulent length scales, λ_t, must be comparable to or greater than the beam field ($\lambda_t > 2R\tan\theta$, where R is the vertical distance from the transducer head to the ADCP range cell) in order to be resolvable using adjacent beam covariances ($\overline{b'_i b'_j}$).

The applicability of Eqs. (2)–(4) is limited by various sources of error, including measurement uncertainties, misalignment errors, and wave-induced biases. In particular, the horizontal beam separation length scale imposes a limit on the smallest turbulent motions that can be resolved via Eq. (4), which affects the estimation of the lateral stresses. However, we expect that beam covariances will have an appreciable signal if the dominant turbulent motions remain larger than the beam field. For the vertical stress components, turbulent motions with less than twice the vertical bin size will not be detectable by the variance method (Eqs. 2 and 3) (Stacey et al. 1999b); this can result in the underestimation of turbulent stresses, especially under strongly stratified conditions (Kirincich et al. 2010). As noted earlier, we expect the effects of stratification to be negligible for our observations (*see* Section: *Field deployment*). In Section: *Wave-turbulence decomposition*, we discuss methods to isolate the turbulence spectrum and remove wave-induced errors from ADCP-based Reynolds stress estimates. We examine the effects of misalignment errors and measurement uncertainties in Sections: *Alignment errors* and *Uncertainty in stress measurements*, respectively.

Wave-turbulence decomposition

To compute ADCP-derived Reynolds stress estimates, raw along-beam velocities were segmented into 20 min windows with a 50% (10 min) overlap. Following Emery and Thomson (1997), measurements near the sea surface boundary

(top $\sim 10\%$ of the water column) were excluded to prevent acoustic sidelobe contamination. Along-beam velocities smaller than the ADCP error velocities were rejected and replaced with interpolated values. Data records (20-min intervals) in which the fraction of interpolated pings exceeded 15% of the total number of data points were excluded from the analysis.

Following the work of Kirincich et al. (2010) and extending it to include the lateral stress term, we rewrite Eqs. (2)–(4) in spectral form as

$$Co_{u'w'}(f) = \frac{S_{b'_2 b'_2}(f) - S_{b'_1 b'_1}(f)}{4\sin\theta\,\cos\theta} \quad (5)$$

$$Co_{v'w'}(f) = \frac{S_{b'_4 b'_4}(f) - S_{b'_3 b'_3}(f)}{4\sin\theta\,\cos\theta} \quad (6)$$

$$Co_{u'v'}(f) = \frac{S_{b'_1 b'_3}(f) - S_{b'_1 b'_4}(f) - S_{b'_2 b'_3}(f) + S_{b'_2 b'_4}(f)}{4\sin^2\theta} \quad (7)$$

where $S_{b'_i b'_i}(f)$ and $S_{b'_i b'_j}(f)$ represent the along beam velocity fluctuation spectra and adjacent beam fluctuation cospectra, respectively. For each 20 min burst, we compute the spectral quantities [$S_{b'_i b'_i}(f)$ and $S_{b'_i b'_j}(f)$] in Eqs. (5)–(7) from quality-controlled, de-meaned along-beam velocities (e.g., $b'_i = b_i - \overline{b_i}$) using a single Hanning-tapered window, and derive estimates of the horizontal wave velocities (σ_w) and vertical wave velocity pseudo-spectra ($\widehat{S}_{ww}$) from ADCP pressure data via linear wave theory.

We focus below on an example drawn from a 20-min burst at a single depth cell located 3.8 m above the bed to illustrate the wave-turbulence decomposition technique for the lateral stress cospectra (Fig. 3). To isolate the low-frequency (below the waveband) turbulent fluctuations from the surface gravity wave-induced motions, we apply a waveband cutoff frequency, f_{wc} (*see* vertical dot-dash line in Fig. 3). The waveband cutoff is defined by the frequency at which the pressure-based vertical velocity pseudo-spectrum, $\widehat{S}_{ww}$ (Fig. 3a), exceeds the mean along-beam velocity spectrum ($\overline{S_{b'_i b'_i}}$) (Gerbi et al. 2008; Kirincich et al. 2010). Below this cutoff ($f < f_{wc}$), the velocity cospectra (Fig. 3b) are assumed to be dominated by turbulent motions. As noted in Section: *Stress estimates from ADCP measurements*, the beam separation scale limits the smallest turbulent motions that can be resolved by the Janus ADCP. Therefore, a high frequency limit $f \leq |v_c| / (2R\tan\theta)$, where $|v_c|$ is the local time-averaged horizontal velocity magnitude, is also applied to ensure that analysis of the below-waveband lateral stress cospectra excludes frequencies greater than those corresponding to the beam separation length scale (*see* vertical dashed line in Fig. 3).

Below-waveband Reynolds stress estimates are thus obtained by integrating Eqs. (5)–(7) as follows:
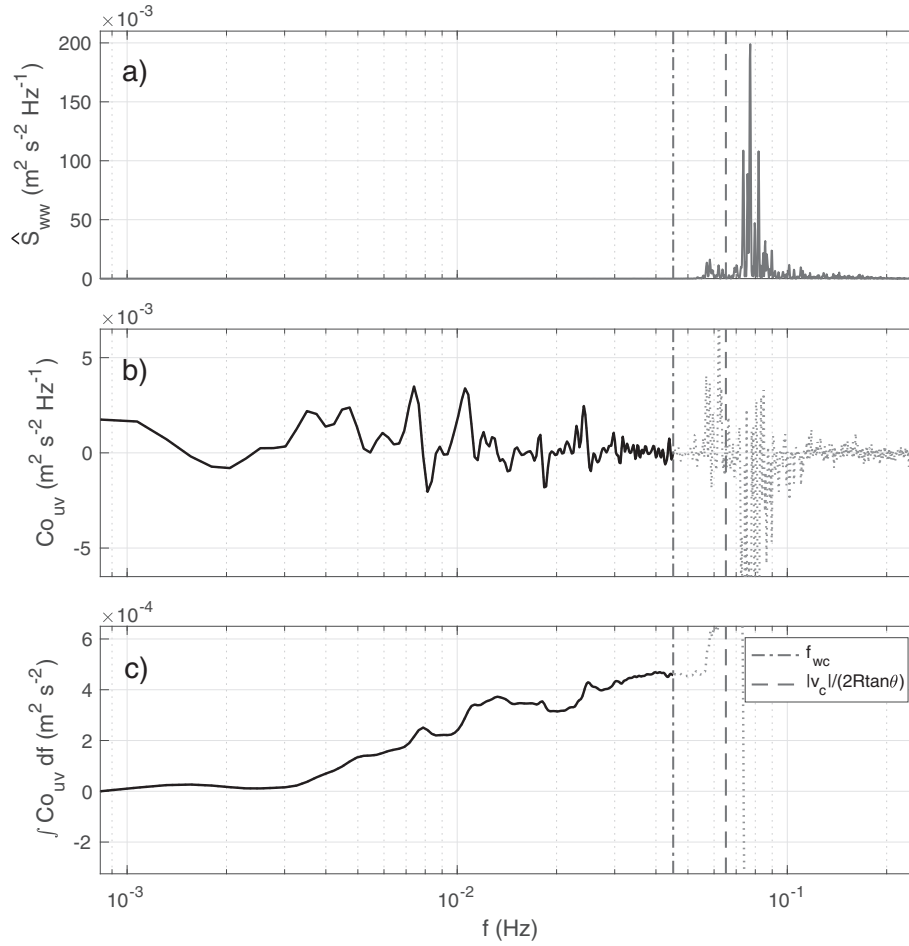
Fig. 3. Wave-turbulence decomposition technique applied to a 20-min sample burst, 3.8 m above the seabed at ADCP 12N: (**a**) vertical velocity pseudo-spectra ($\widehat{S}_{ww}$) derived from pressure spectra, (**b**) lateral turbulent stress cospectra derived from Eq. (7), and (**c**) integrated turbulent stress cospectra (ogive curves). Vertical dot-dashed and dashed lines indicate the wave cutoff frequency (f_{wc}) and the beam separation frequency ($|v_c|/(2R\tan\theta)$), respectively. Dashed gray indicate data not included in the analysis due to these cutoffs.

$$\overline{u'_i u'}_{j\,\mathrm{LF}} = \int_{f_{i1}}^{f_{i2}} Co_{u_{i'} u_{j'}} \, df \qquad (8)$$

where f_{i1} and f_{i2} are the lower and upper frequency limits, respectively. For vertical stress cospectra, $f_{i2} = f_{wc}$. For lateral stress cospectra, f_{i2} is given by the lowest of the upper frequency limits: f_{wc} or $|v_c|/(2R\tan\theta)$. For all cases, f_{i1} corresponds the minimum frequency that can be resolved by a 20-min time window (i.e., $\sim 8.3 \times 10^{-4}$ Hz). The integral in Eq. (8) is calculated using a trapezoidal method (Fig. 3c).

If applied correctly, the spectral wave-turbulence decomposition technique described above should not suffer from wave biases because it relies only on the low-frequency (below the waveband) portion of the turbulence cospectrum to estimate the turbulent stresses. However, the proposed technique avoids these wave biases at the expense of neglecting the turbulent stresses that reside within the waveband. Also, below-waveband spectra can be altered where the wave motion is substantial due to the effects of wave advection (Rosman and Gerbi 2017). Therefore,

screening criteria were applied to ensure that most of the turbulent stress is contained below the wave cutoff frequency (*see* Section: *Screening criteria*) and to limit the kinematic effects of wave induced advection on the observed cospectra. These quality controlled, below-waveband covariances should be nearly the same as the actual Reynolds stresses, but slightly smaller. Screening procedures are described in Section: *Screening criteria*.

Alignment errors

In practice, the ADCP reference frame is often slightly misaligned from the "true" (*x*, *y*, *z*) coordinate system. Here, the true coordinate system refers to a reference frame that is vertically aligned with gravity and parallel to the principal axes of the flow. Instrument tilt angles or an imperfect alignment with the principal flow axes can introduce biases in the estimation of turbulent stresses, even in the absence of waves. The following analysis is focused on the turbulence biases arising from small sensor misalignments at frequencies below the waveband. At higher frequencies, we expect that wave biases will overwhelm both the alignment errors and the stress

measurements as noted by Trowbridge (1998) and Shaw and Trowbridge (2001). Hence, the analysis herein only applies to misalignment errors resulting from low-frequency (below the waveband) covariances.

Assuming small angle rotations ($\sin\psi \sim \psi$, $\cos\psi \sim 1$) and retaining only the first-order terms ($\psi^2 \ll 1$), we can derive an expression for the instrument velocities (u_I, v_I, w_I) in terms of the true velocities (u, v, w) (Rosman et al. 2008)

$$\begin{bmatrix} u_I \\ v_I \\ w_I \end{bmatrix} = \begin{bmatrix} 1 & \psi_H & -\psi_R \\ -\psi_H & 1 & \psi_P \\ \psi_R & -\psi_P & 1 \end{bmatrix} \begin{bmatrix} u \\ v \\ w \end{bmatrix} \quad (9)$$

where ψ_P, ψ_R, and ψ_H are the instrument pitch, roll, and heading angles (in radians), respectively, and represent rotations about the "true" x, y, and z axes (positive counterclockwise). With this, Eqs. (2)–(4) become

$$\frac{\overline{b_1'^2} - \overline{b_2'^2}}{4\sin\theta\cos\theta} = -\overline{u'w'} + \psi_R\left(\overline{w'^2} - \overline{u'^2}\right) + \psi_P\overline{u'v'} - \psi_H\overline{v'w'} \quad (10)$$

$$\frac{\overline{b_3'^2} - \overline{b_4'^2}}{4\sin\theta\cos\theta} = -\overline{v'w'} + \psi_P\left(\overline{v'^2} - \overline{w'^2}\right) + \psi_H\overline{u'w'} - \psi_R\overline{u'v'} \quad (11)$$

$$\frac{\overline{b_1'b_4'} - \overline{b_1'b_3'} - \overline{b_2'b_4'} + \overline{b_2'b_3'}}{4\sin^2\theta} = -\overline{u'v'} + \psi_H\left(\overline{u'^2} - \overline{v'^2}\right) + \psi_R\overline{v'w'} \\ - \psi_P\overline{u'w'} \quad (12)$$

For unstratified open-channel flows with smooth beds and high Reynolds numbers, Nezu and Nakagawa (1993) (*see* also, Stacey et al. 1999a) give $\overline{v'^2} \approx 5.29 u_*^2$, $\overline{u'^2} \approx 2.66 u_*^2$, and $\overline{w'^2} \approx 1.61 u_*^2$, where u_* is the friction velocity. If we further assume that $\overline{u'w'} \ll \overline{v'w'} \sim \overline{u'v'} \sim u_*^2$ and that turbulent intensities ($\overline{u'^2}$, $\overline{v'^2}$, $\overline{w'^2}$) and Reynolds stresses are in phase throughout the tidal cycle (observations in Section: *Reynolds stress estimates* will establish that these assumptions are valid in our case), then the alignment error for the vertical and lateral stress components reduces to $\epsilon_{vw} \sim (3.7\psi_P \pm \psi_R)\overline{v'w'}$ and $\epsilon_{uv} \sim (2.6\psi_H \pm \psi_R)\overline{u'v'}$ for the smooth wall case. Given our pitch, roll, and heading values, this can result in worst-case biases (ϵ_{vw}) as high as 14% and 26% of the total $\overline{v'w'}$ stress for the 12N and 12S ADCPs, respectively (*see* Table 1 for rotation angles). For the lateral stress, the estimated alignment biases (ϵ_{uv}) can be up to 11% and 21% of the total $\overline{u'v'}$ stress at the 12N and 12S ADCPs, respectively. For rough beds such as coral reefs, however, we anticipate a reduction in the level of anisotropy relative to the smooth wall case (Nezu and Nakagawa 1993; Smalley et al. 2002). This is because bottom roughness tends to redistribute turbulent energy toward isotropy, thus reducing the difference between velocity variances (e.g., $\overline{u'^2} - \overline{v'^2} \to 0$). Alignment biases should therefore decrease

for both the vertical and horizontal stresses as anisotropy decreases and turbulent intensities become more comparable.

Uncertainty in stress measurements

The uncertainty error in the stress measurements via Eqs. (3) and (4) is defined by the variance of these equations (Stacey et al. 1999a). A number of techniques have been developed to quantify uncertainty in ADCP-derived Reynolds stress estimates. Here, we compute uncertainty estimates for both vertical and lateral below-waveband Reynolds stresses by adapting two different approaches developed by Williams and Simpson (2004) and Lu and Lueck (1999).

Following Williams and Simpson (2004), the variance of Eqs. (3) and (4) is given by

$$\text{var}\left(-\widehat{v'w'}\right) = \sigma_{vw}^2 = \frac{\text{var}\left(\widehat{b_3'^2} - \widehat{b_4'^2}\right)}{16\sin^2\theta\cos^2\theta} \quad (13)$$

$$\text{var}\left(-\widehat{u'v'}\right) = \sigma_{uv}^2 = \frac{\text{var}\left(\widehat{b_1'b_4'} - \widehat{b_1'b_3'} - \widehat{b_2'b_4'} + \widehat{b_2'b_3'}\right)}{16\sin^4\theta} \quad (14)$$

where the hat operator represents an estimator of the expected value. These expressions can be expanded using the additive rule for covariances and the central limit theorem (e.g., $\text{var}\left(\widehat{b_i'^2}\right) = (1/N)\sum_{n=1}^{N} b_i'^2(n) = \text{var}\left(b_i'^2\right)/N$) to give

$$\sigma_{vw}^2 = \frac{\gamma_{vw}}{16N\sin^2\theta\cos^2\theta}\left[\text{var}\left(b_3'^2\right) + \text{var}\left(b_4'^2\right) - 2\text{cov}\left(b_3'^2, b_4'^2\right)\right] \quad (15)$$

$$\begin{aligned}\sigma_{uv}^2 = \frac{\gamma_{uv}}{16N\sin^4\theta}[&\text{var}(b_1'b_4') + \text{var}(b_1'b_3') + \text{var}(b_2'b_4') + \text{var}(b_2'b_2') \\ &- 2\text{cov}(b_1'b_4', b_1'b_3') - 2\text{cov}(b_1'b_4', b_2'b_4') \\ &+ 2\text{cov}(b_1'b_4', b_2'b_3') + 2\text{cov}(b_1'b_3', b_2'b_4') \\ &- 2\text{cov}(b_1'b_3', b_2'b_3') - 2\text{cov}(b_2'b_4', b_2'b_2')]\end{aligned} \quad (16)$$

where $N = 600$ is the number of measurements in each burst, $\gamma_{u_iu_j}$ is a correction factor

$$\gamma_{u_iu_j} = 1 + 2\sum_{n=2}^{K} C_{bb}(1, n) \quad (17)$$

that accounts for the correlation of consecutive non-independent samples (Williams and Simpson 2004), C_{bb} is a normalized autocovariance function for the square of the along-beam velocity fluctuations

$$C_{bb}(1, m) = \frac{\sum_{n=1}^{N-1}\sum_{m=n+1}^{N} b_i'^2(n), b_i'^2(m)}{\sum_{n=1}^{N}\text{var}\left[b_i'^2(n)\right]} \quad (18)$$

The upper limit $m = K \ll N$ in Eq. (17) is defined as the lag at which C_{bb} crosses the upper bound of its uncertainty level. For sufficiently large K values (typically > 30 s), the along-beam velocity fluctuations become uncorrelated and $C_{bb} \to 0$. To compute C_{bb}, we low-pass filter the along-beam fluctuations using the wave cutoff frequency (f_{wc}) to attenuate wave-induced velocities. The factor $\gamma_{u_i u_j}$ was similar for both vertical and lateral stresses, and varied between 14 and 10 for peak and slack velocities, respectively.

Reynolds stress uncertainty estimates were also computed directly from the data using a Monte Carlo type approach following Lu and Lueck (1999) (*see* also, Kirincich et al. 2010). In this case, we rearrange Eqs. (3) and (4) into an equivalent covariance form

$$\frac{\overline{b'^2_3} - \overline{b'^2_4}}{4\sin\theta\cos\theta} = \frac{\overline{(b'_3 + b'_4)(b'_3 - b'_4)}}{4\sin\theta\cos\theta} \tag{19}$$

$$\frac{\overline{b'_1 b'_4} - \overline{b'_1 b'_3} - \overline{b'_2 b'_4} + \overline{b'_2 b'_3}}{4\sin^2\theta} = \frac{\overline{(b'_1 - b'_2)(b'_4 - b'_3)}}{4\sin^2\theta} \tag{20}$$

and randomly shift one time series (e.g., $(b'_1 - b'_2)$) with respect to the other (e.g., $(b'_4 - b'_3)$) by a lag (or lead) greater than the along-beam decorrelation timescale. This essentially decouples the signals but preserves the statistical nature of the burst. Similar to Eq. (18), we compute the decorrelation timescale using along-beam, low-pass filtered (below the waveband) velocity fluctuations. Decorrelation timescales ranged between 15 and 80 s for peak and slack velocities, respectively. We then shift these signals 1000 times using random lags greater than the decorrelation times and compute below-waveband covariances for each realization to produce distributions of lagged covariances (or "zero covariance histograms"). These lagged covariance histograms are normally distributed around zero (e.g., *see* fig. 1 in Lu and Lueck (1999) and allow us to test if a stress estimate is statistically different from zero. Stress uncertainties are estimated as two standard deviations (2σ) of the zero covariance histogram for each 20-min burst. Stress estimates that exceed the 2σ level are considered statistically significant.

Figure 4 shows quality controlled (*see* Section: *Screening criteria*) uncertainty estimates for the below-waveband turbulent stresses, defined here as two standard deviations (2σ), as a function of the below-waveband Reynolds stress estimates ($\overline{u'_i u'_j}_{LF}$). Binned average uncertainties obtained via methods outlined by Lu and Lueck (1999) (black circles) and Williams and Simpson (2004) (white squares) were in close agreement for all datasets. Consistent with previous observations (e.g., Williams and Simpson 2004; Rosman et al. 2008; Kirincich et al. 2010), mean uncertainties increase with the magnitude of the stress. Using a least-squares fit, the minimum uncertainty levels for vertical and lateral stresses were estimated as 2.1×10^{-5} m^2 s^{-2} and 5.5×10^{-5} m^2 s^{-2}, respectively. The ratio $\sigma_{u'v'}/\sigma_{v'w'}$ was on average ~ 2.8 over the entire

range and did not show any meaningful dependence on flow speed, flow direction, or stress magnitudes. This ratio is likely the result of the ADCP beam geometry, as the ratio of the values in the denominator of Eqs. (3) and (4) yields $(\sin\theta\cos\theta)/(\sin^2\theta) \approx 2.75$ for $\theta = 20°$.

As noted by Nidzieko et al. (2006), accurate ADCP estimates of Reynolds stress are possible when the stress estimates are discernible from the background noise. Using the 2σ criteria, about 88% of the raw $\overline{u'v'}$ data fall beneath the noise floor (raw data above the black line in Fig. 4c,d). This in contrast to the $\overline{v'w'}$ stress measurements, which clearly have a lower noise floor and exhibit lower uncertainties overall ($\sim 60\%$ of the raw data are below the noise floor and above the black line in Fig. 4a,b). In Section: *Phase ensemble averaging*, we will use phase ensemble-averaging to increase the signal-to-noise ratio of our vertical and lateral stress estimates.

Stress estimates from ADV measurements

ADV-derived Reynolds stress estimates were computed directly from velocity cospectra below the waveband, following the wave-turbulence separation method outlined in Section: *Wave-turbulence decomposition*, to enable comparisons with ADCP values. ADV velocities were rotated into the right handed (x, y, z) coordinate system shown in Fig. 1, so that u and v velocities were aligned with the depth-averaged cross- and alongshore flow, respectively (w was upward positive). Velocity data were de-spiked and poor data quality points with correlations < 0.7 were rejected (Feddersen and Williams 2007). Data gaps with less than 8 consecutive invalid data points (0.5 s) were linearly interpolated. Reynolds stress estimates were computed hourly using an averaging interval equivalent to the ADV sampling window (16 and 12 min for 12N and 12S ADVs, respectively). While the ADCPs and ADVs use different averaging intervals (20 min for ADCPs), we can use phase ensemble-averaging (Section: *Phase ensemble averaging*) to enable robust comparisons.

Results

Application of the methodology

Phase ensemble averaging

Given the regularly periodic alongshore velocities resulting from the dominant semidiurnal tidal pattern observed at Makua (*see* Fig. 2), it is convenient to examine the turbulent properties of the flow as a function of tidal phase. We therefore employ an ensemble-averaging approach to increase the reliability of ADCP-derived turbulent quantities and provide a more robust measure of the vertical structure and temporal evolution of the turbulent stress estimates. The phase ensemble-averaging procedure is similar to the one described by Arzeno et al. (2018) and Amador et al. (2020), with some minor modifications. In this case, we extract the tidal phase (ϕ) for each site (12N, 12S) from depth-averaged along-shore velocity via complex demodulation (Emery and
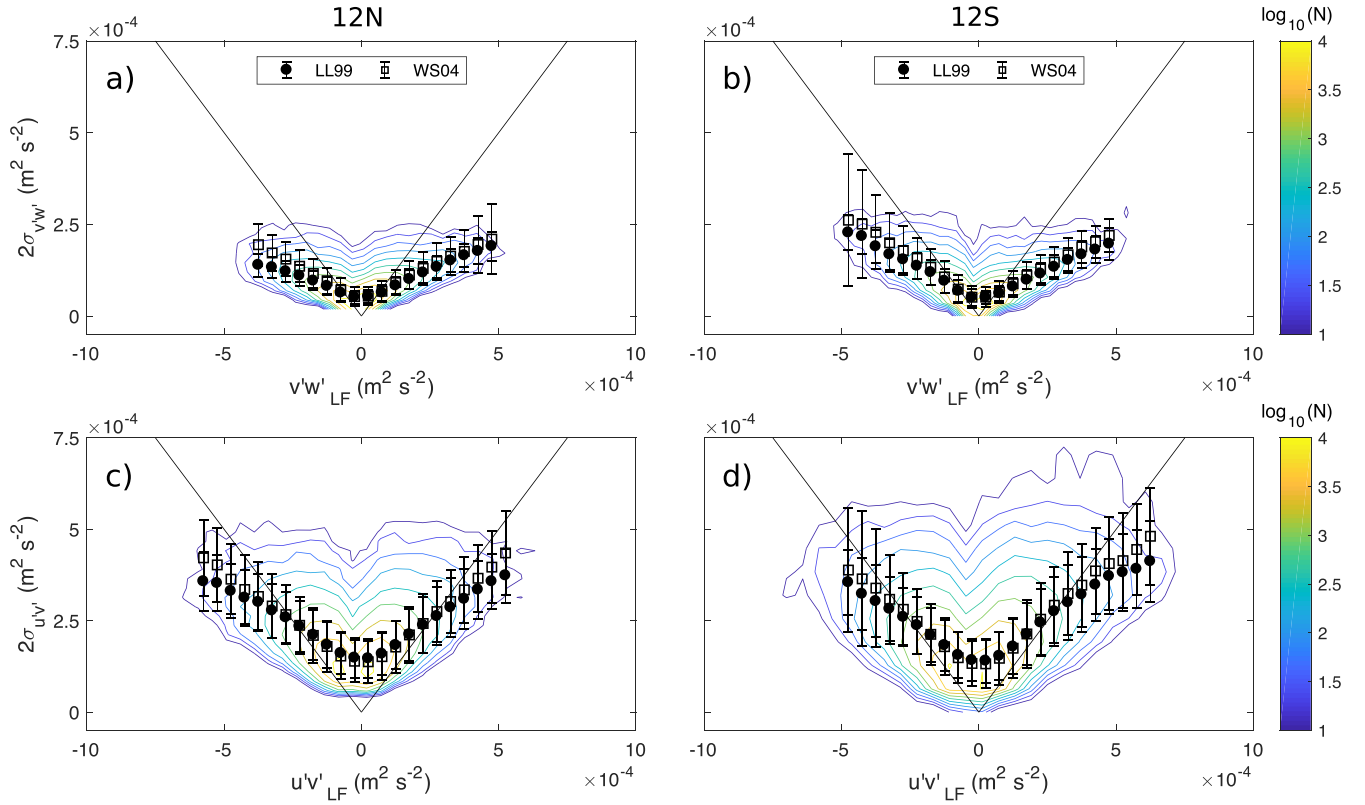
Fig. 4. Contoured (raw) and binned-averaged cospectra uncertainty estimates ($2\sigma_{u_{i'}u_{j'}}$) via methods proposed by Lu and Lueck (1999) (black circles) and Williams and Simpson (2004) (white squares), plotted against the zero-lag, below-waveband covariance ($\overline{u_{i'}u_{j'}}_{LF}$) for (**a,c**) 12N and (**b,d**) 12S ADCPs. Uncertainty estimates are defined as two standard deviations (2σ). Contour lines illustrate the raw data distribution as $\log_{10}(N)$, where N represents the number of values. Error bars indicate the standard deviation for each bin average. Stress levels become larger than the uncertainty estimates below the solid black lines.

Thomson 1997) using a filter centered on the M_2 tidal frequency band (12:42 h). The tidal phase (ϕ) is defined so that the interval between maximum depth-averaged northward currents follows linearly from 0° to 360° in 5° increments for each tidal cycle. Cross- and alongshore velocity measurements, vertical shear, sea surface height, turbulence cospectra, and Reynolds stress estimates are then phase-averaged over 50 tidal cycles using 10° phase blocks.

Turbulence cospectra and roll-off wavenumbers

We can examine the turbulence cospectra to gain some insight into the quality of the Reynolds stress estimates and to calculate the roll-off wavenumber (k_0), which is associated with the horizontal length scale of the dominant stress-carrying eddies ($\lambda_0 = 2\pi/k_0$). Here, we consider ADCP-based variance-preserving cospectra [$kCo(k)_{u_{i'}u_{j'}}$] and ogive curves [$\int^k Co_{u_{i'}u_{j'}}(\hat{k}) \, d\hat{k}$] for both lateral ($i = 1$, $j = 2$) and vertical ($i = 2$, $j = 3$) stress components. The ogive curves represent the cumulative integral of the turbulence cospectra. The location of the roll-off wavenumber (k_0) is represented by the peak

in the variance-preserving cospectrum or, equivalently, by the inflection point in the ogive curve.

To estimate k_0, observed frequency cospectra [$Co_{u_{i'}u_{j'}}(f)$] are computed using Eqs. (6) and (7) and converted to wavenumber cospectra [$Co_{u_{i'}u_{j'}}(k)$] using a frozen turbulence approximation $2\pi f = k|v_c|$, where v_c represents the local mean horizontal velocity for each 20-min burst. We omit data within the waveband using the wave-turbulence decomposition technique described in Section: *Wave-turbulence decomposition*, and only consider cases when $\sigma_w/|v_c| < 2$. To minimize the effects of noise in individual cospectra, integrated cospectra (ogive curves) are normalized by the below-waveband covariance

$$Og_{u_{i'}u_{j'}}(k) = \frac{\int^k Co_{u_{i'}u_{j'}}(\hat{k}) \, d\hat{k}}{\overline{u_{i'}u_{j'}}_{LF}}$$

and grouped together by depth cell (z) and tidal phase (ϕ) using 10° phase blocks (*see* Section: *Phase ensemble averaging*).

Phase ensemble-averages of multiple $Og_{u_i'u_j'}(k)$ realizations reduce the effects of spectral noise and enable smoother cospectral estimates. This allows the estimation of a representative roll-off wavenumber (k_0) via the inflection point in the ogive ensemble without assuming any particular cospectral shape. The inflection point is determined from a least-squares spline fit to the $Og_{u_i'u_j'}(k)$ ensemble (composed of around 60–80 individual realizations) at each phase and depth bin. Anomalous ogive curves with a standard deviation exceeding the standard deviation of the ensemble by more than a factor of three are classified as outliers and rejected from the analysis (*see* Section: *Screening criteria*).

To assess the spectral distribution of the lateral and vertical stress components, we compute ensemble-averaged estimates of the nondimensional variance-preserving cospectra (Fig. 5a–d) and the associated ogive curves (Fig. 5e–h) as a function of nondimensional wavenumber (k/k_0) for the 12N and 12S ADCPs. The displayed quantities in Fig. 5 (black circles) have been normalized and averaged considering all data points. Prior to averaging, all of the individual nondimensional ogives ($Og_{u_i'u_j'}$) and variance-preserving cospectra ($kCo_{u_i'u_j'}/\overline{u_i'u_j'}_{LF}$) are grouped into logarithmically-spaced normalized wavenumber (k/k_0) bins. The resulting spectral stress distributions collapse according to the roll-off wavenumber (k_0), a quantity that varies with tidal phase in this case (*see* Section: *Turbulence length scales*).

The observed cospectral estimates can be compared to more familiar Kaimal et al. (1972) model

$$Co^*_{v'w'}(k)/\overline{v'w'} = \left(\frac{7}{3\pi}\sin\frac{3\pi}{7}\right)\frac{1/k_0}{1+(k/k_0)^{7/3}} \tag{21}$$

stated here for the *y–z* plane. The Kaimal model is a semi-theoretical prediction of the one-dimensional turbulence cospectra derived from observations of the atmospheric boundary layer. While previous studies have successfully applied the Kaimal model in a variety of oceanographic settings as a tool to filter out wave contributions from vertical turbulent cospectra (e.g., Feddersen and Williams 2007; Gerbi et al. 2008; Kirincich et al. 2010), the validity of using Eq. (21) for characterizing the lateral turbulent cospectra is questionable because the associated spectral stress distribution has not been previously examined. Hence, the plots in Fig. 5 show the variance preserving and ogive curves derived from the nondimensional Kaimal model (gray curves) for reference only.

Normalized variance-preserving plots for both the vertical (Fig. 5a,b) and lateral (Fig. 5c,d) stress components show general agreement with the Kaimal model at the 12N and 12S sites. Slight deviations between the measured and the model cospectra can be observed at low and high wavenumbers, with lower covariances for the measured values near the peak ($k/k_0 = 1$). Some of the observed deviations may be

attributable to random inaccuracies in the estimation of k_0 or spectral scatter around k_0. Note also that the lateral stress cospectra exhibit greater uncertainties than their vertical counterparts, consistent with uncertainty estimates obtained in Section: *Uncertainty in stress measurements*. Despite these limitations, our findings indicate that the lateral stress cospectra at both sites (Fig. 5c,d) have relatively higher energy near the inflection point ($k/k_0 = 1$) and drop off more abruptly at higher wavenumbers [$0.1 \lesssim \log_{10}(k/k_0) \lesssim 0.6$] than the vertical stress cospectra, with correspondingly steeper nondimensional ogive curves (Fig. 5g,h). As reported by Gerbi et al. (2008) and Kirincich et al. (2010), the nondimensional ogive curves corresponding to the vertical stress (Fig. 5e,f) fall close to the Kaimal model.

Screening criteria

The k_0 values obtained above (Section: *Turbulence cospectra and roll-off wavenumbers*) along with the mean current speed and the surface wave conditions can be used to diagnose the effects of wave advection on turbulence cospectra, and to provide guidance about the viability of the Reynolds stress estimates. Recent results by Rosman and Gerbi (2017) indicate that the observed below-waveband turbulent cospectra remains relatively unaffected by wave orbital motion when rms (root mean square) wave orbital velocities (σ_w) are less than twice the current speed $\sigma_w/|v_c| < 2$, and when the wave orbital excursion is smaller than the length scale of the stress-carrying eddies $\sigma_w k_0/\omega_w < 0.5$, where ω_w represents the peak wave radian frequency. Under such conditions, over 80% of the turbulence covariance is expected to reside in frequencies below the wave peak, and about 60% of the total stress covariance should be contained at frequencies below the turbulence roll-off frequency ($f_0 = k_0|v_c|/2\pi$), assuming a Kaimal spectrum (Eq. 21) (Rosman and Gerbi 2017). To ensure that most of the turbulence covariance is contained below the wave cutoff frequency (f_{wc}), we therefore restrict our observations to instances when $\sigma_w/|v_c| < 2$ and $\sigma_w k_0/\omega_w < 0.5$. In addition, as noted in Section *Turbulence cospectra and roll-off wavenumbers*, we reject bursts if the normalized ogive curve standard deviation is three times greater than that of the phase ensemble.

Histograms in Fig. 6a,b show that most of the bursts (73% and 77% for 12N and 12S, respectively) lie below the $\sigma_w/|v_c| < 2$ threshold. Histograms in Fig. 6c,d show the distribution of quality-controlled data ($\sigma_w/|v_c| < 2$ and $\sigma_w k_0/\omega_w < 0.5$) as a function of $\sigma_w k_0/\omega_w$ for the vertical ($\overline{v'w'}$) and lateral ($\overline{u'v'}$) stress components. It should be noted that applying the $\sigma_w k_0/\omega_w < 0.5$ criteria a posteriori does not increase the amount of rejections by more than 2% for either stress component. On the other hand, the ogive standard deviation criteria (described above in Section: *Turbulence cospectra and roll-off wavenumbers*) further limits the amount of valid vertical and lateral stress measurements, respectively, to 62% and 54% of the total bursts at 12N, and to 66% and 58% of the total bursts at 12S.
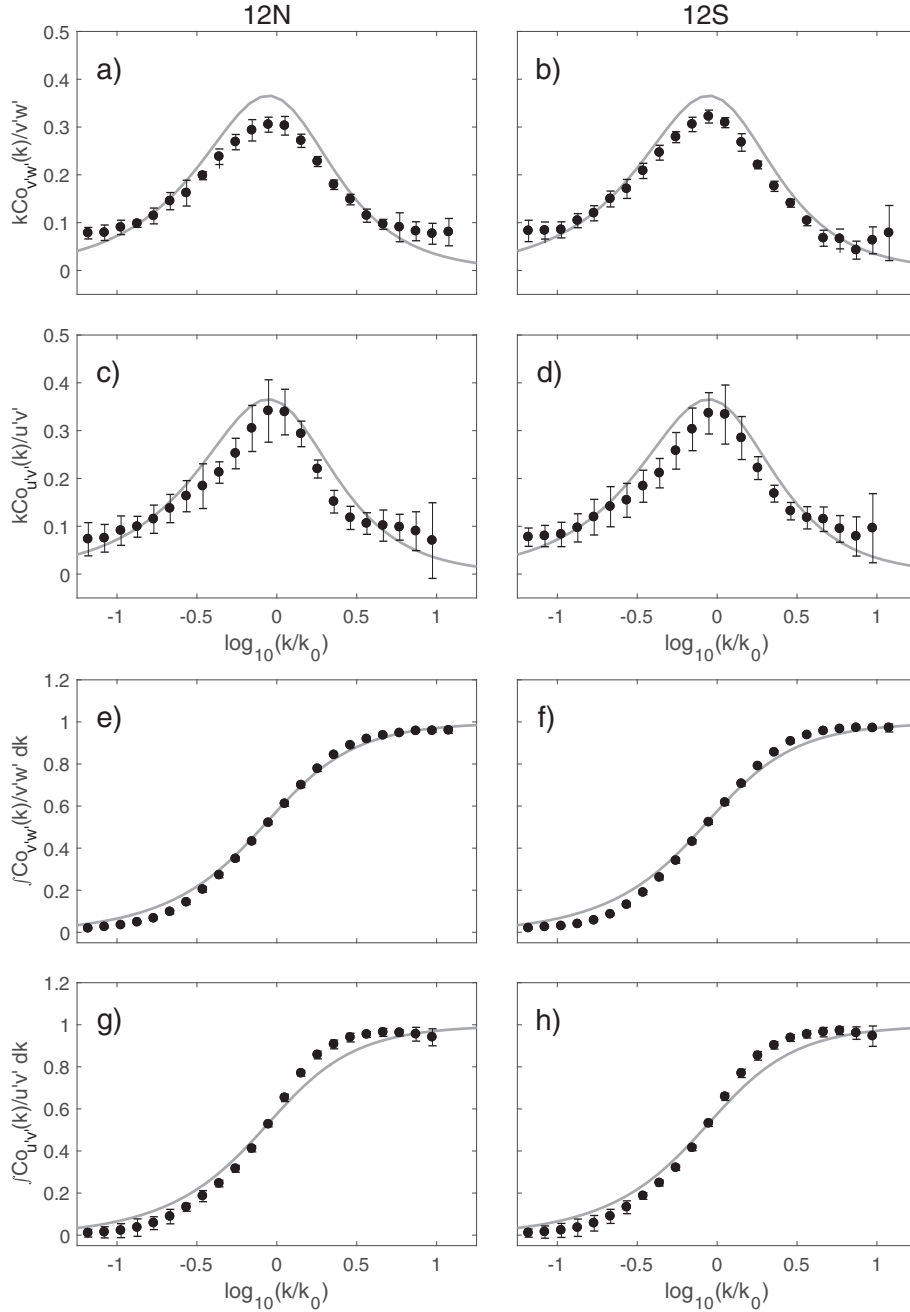
Fig. 5. Normalized variance-preserving cospectra (**a–d**) and ogive curves (**e–h**) as a function of normalized wavenumber (k/k_0) for the 12N (left panels) and 12S (right panels) ADCPs. Panels (**a,b,e,f**) and (**c,d,g,h**) show results for vertical and lateral stress cospectra, respectively. Black dots represent bin averages of all the observations. Vertical error bars show the 95% confidence intervals estimated using a bootstrapped method. The solid gray curves show the Kaimal model (21) for reference.

Finally, to determine whether the influence of infragravity motions affect the lateral stress estimates, horizontal velocity fluctuations were computed from measured pressure spectra in the infragravity band (30 s to 20 min) via linear wave theory. More specifically, we infer the non-turbulent horizontal velocity variances, $(\widetilde{u}\widetilde{u})_{IG}$, in the infragravity band from

$$\widehat{S}_{\widetilde{u}\widetilde{u}}\left(z_{\widetilde{u}}f\right) = S_{pp}(z_p,f)\left[\frac{k}{\rho\omega}\frac{\cosh\left(k\left(z_{\widetilde{u}}+h\right)\right)}{\cosh\left(k(z_p+h)\right)}\right]^2$$

$$\widetilde{u}\widetilde{u}_{IG}\left(z_{\widetilde{u}}\right) = \int^{f_{IG}}\widehat{S}_{\widetilde{u}\widetilde{u}}\left(z_{\widetilde{u}}f\right)\,\mathrm{d}f$$
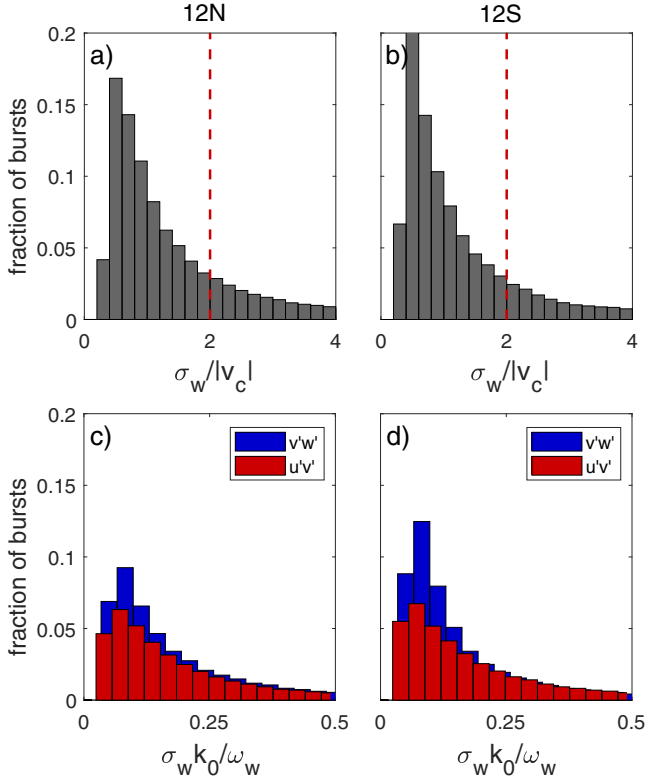
Fig. 6. Screening criteria for the spectral wave-turbulence decomposition method for (**a, c**) 12N and (**b,d**) 12S ADCPs. Panels (**a**) and (**b**) show histograms of the wave advection to current speed ratio ($\sigma_w/|v_c|$) for the observational period, with the cutoff marked with a red dashed line. Panels (**c**) and (**d**) show histograms of the ratio of wave orbital excursion to estimated turbulence length scale ($\sigma_w k_0/\omega_w$) for quality controlled bursts with $\sigma_w/|v_c| < 2$ and $\sigma_w k_0/\omega_w < 0.5$ for the vertical (blue) and lateral (red) stress components.

where z_p and $z_{\widetilde{u'}}$, respectively, represent the depth for the pressure measurements and the velocity calculations, f_{IG} are the frequencies associated with the infragravity band, and $\widehat{S}_{\widetilde{u}\widetilde{u}}$ is the horizontal velocity pseudo-spectra derived from the measured pressure spectra (S_{pp}). Comparison of these infragravity velocity variances with the lateral stress covariances indicates that the non-turbulent velocity fluctuations provide a negligible contribution to the below-waveband stress estimates, with infragravity variances seldom exceeding 5% of the stress values (< 2% on average).

Reynolds stresses

Turbulence length scales

As described in Section: *Turbulence cospectra and roll-off wavenumbers*, the roll-off length scales (λ_0) are estimated empirically from phase-averaged ogive curves (below the waveband) using the frozen turbulence hypothesis, and represent the horizontal (in the direction of the mean current) length scale of the dominant stress-carrying eddies.

Figure 7 shows the roll-off length scales ($\lambda_0 = 2\pi/k_0$) derived from vertical (Fig. 7a) and lateral (Fig. 7b) turbulent cospectra as a function of range and tidal phase (ϕ) for the 12S ADCP (similar patterns with phase are observed at 12N). Several features are evident from the phase ensemble-averaged estimates of $\lambda_{0v'w'}$ and $\lambda_{0u'v'}$. In all cases, the roll-off length scales show a similar behavior with tidal phase, varying approximately in phase with the mean alongshore flow (*see* Fig. 9e,f). These roll-off length scales were estimated to be one to four times larger than the depth of the water column, with timescales of around 1–3 min, and always exceeded their vertical distance to the seabed. As shown in Fig. 7, the estimated dominant turbulence length scales were always greater than their respective cutoff values by at least a factor of two. Comparisons between $\lambda_{0v'w'}$ and $\lambda_{0u'v'}$ indicate that the turbulent motions associated with the vertical stress cospectra (Fig. 7a) were coherent over longer length scales (between 20% and 50% longer) than those associated with the lateral stress cospectra (Fig. 7b) at maximum currents ($\phi \approx 0°$, $\phi \approx 180°$). For slack water ($\phi \approx 90°$, $\phi \approx 270°$), the turbulent length scales were found to be comparable. Weak vertical variability is observed for both quantities, consistent with observations by Stacey et al. (1999a) and Kirincich et al. (2010). The vertical structure of $\lambda_{0v'w'}$ and $\lambda_{0u'v'}$ is shown in Fig. S5.

A similar behavior is observed for both $\lambda_{0v'w'}$ and $\lambda_{0u'v'}$ throughout the tidal cycle, suggesting a correspondence between the vertical ($\lambda_{0v'w'}$) and lateral ($\lambda_{0u'v'}$) turbulent length scales. The observations suggest that $\lambda_{0u'v'} \sim \lambda_{0v'w'} \sim h$, where h is the local water depth. It might be anticipated that $\lambda_{0u'v'}$ should scale with the length scale for lateral changes in velocity. Spatial velocity measurements at Makua (Amador et al. 2020), however, reveal that the alongshore flow changes over lateral scales L_x that are much greater than the observed turbulence length scales. This implies that the turbulent motions associated with bottom-driven turbulence likely dominate the transport of both vertical and lateral turbulent fluxes. It is notable that the streamwise horizontal length scales associated with the peak vertical transport appear to be larger than those that are associated with maximum lateral transport. This observation can be interpreted as an indication that differing horizontal scales can be more effective at transport for different components of momentum. It is unclear from these observations why this might be the case, though this might simply be a consequence of the kinematic relationship between the dominant morphology of turbulent structures and their associated velocity field.

These observations indicate that the dominant stress-carrying eddies are significantly anisotropic, with larger horizontal turbulent length scales than the local water depth. Such large scale turbulent motions have commonly been observed in tidally-driven and inner shelf flows with comparable water depths. For example, Kirincich et al. (2010) estimated the horizontal length scales of the dominant stress-carrying eddies from Reynolds stress cospectra, and found streamwise roll-off
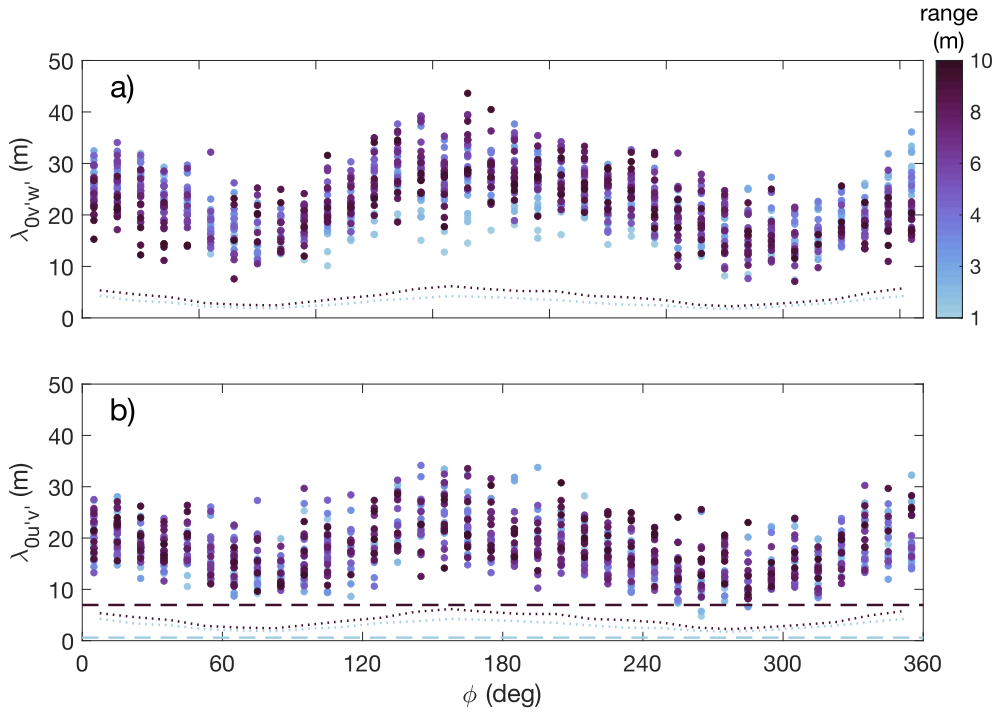
Fig. 7. Phase ensemble-averaged roll-off length scales ($\lambda_0 = 2\pi/k_0$) derived from the (**a**) vertical and (**b**) lateral stress cospectra for ADCP 12S. Colors illustrate the associated ADCP range cell height. Dotted lines in (**a**) and (**b**) show the wave cutoff length scales (λ_{wc}) for the bottom-most (whitish-blue) and uppermost (dark purple) range cells. Dashed lines in (**b**) show the beam separation length scale ($2R\tan(20°)$) for the bottom-most (whitish-blue) and uppermost (dark purple) range cells. Note that values associated with $\overline{v'w'}$ are not subject to the beam separation length scale issue (*see* Section: *Vertical and lateral stress covariances from along-beam velocity fluctuations*).

scales that were considerably larger than the vertical distance to the seabed and that generally exceeded the flow depth. Using current meter triplets in a tidal boundary layer, Gross and Nowell (1985) similarly observed Reynolds stress length scales that were larger than the local water depth. Stacey et al. (1999a) examined the integral length scale of the stress via autocorrelation functions of the along-beam velocities and found horizontal length scales to be notably larger than the vertical scales, again consistent with our results.

Reynolds stress estimates

To assess the performance of ADCP-based Reynolds stress estimates, a comparison with independent, collocated ADV measurements was carried out at 12N and 12S using phase ensemble-averaged data. In Fig. 8, we show the observed below-waveband stress estimates (LF) and cospectra-fit method (Gerbi et al. 2008; Kirincich et al. 2010) estimates (CF) for the vertical (Fig. 8a,b,e,f) and horizontal (Fig. 8c,d, g,h) stress components. Note that we cannot assume that the cospectral shape given by Eq. (21), typically applied for vertical stresses, should apply to lateral stress. While results in Fig. 5c,d,g,h suggest that the Kaimal model adequately describes the low-wavenumber cospectra resulting from the lateral turbulent fluctuations, CF results for $\overline{u'v'}$ cospectra should be interpreted with caution. Comparisons were carried

out using vertically-averaged ADCP data from four depth bins centered around the ADV sampling volume.

As shown in Fig. 8, ADCP-based vertical and lateral stress estimates compare favorably with ADV estimates at both sites. Comparisons between the phase-averaged ADCP- and ADV-based, below-waveband (LF) stress estimates yield r^2 values of 0.85 and 0.67 at 12N, for the vertical ($\overline{v'w'}$) and lateral ($\overline{u'v'}$) stresses, respectively (Fig. 8a–d). Similar results were obtained at 12S, with slightly tighter correlations resulting in r^2 values of 0.94 and 0.85 for $\overline{v'w'}$ and $\overline{u'v'}$, respectively (Fig. 8e–h). Note that below-waveband (LF) and model-derived (CF) stress estimates yield comparable results, providing additional support to the assertion that most of the turbulent covariance is contained below the waveband. As an alternative approach for estimating ADV-based stresses, $\overline{v'w'}$ and $\overline{u'v'}$ were also computed using the "Phase method" (Bricker and Monismith 2007) and compared to the ADCP-based phase-averaged, below-waveband stresses (not shown). Comparisons at 12N resulted in r^2 values of 0.97 and 0.55 for the vertical and lateral stresses, respectively, with slopes of 0.98 and 0.91 and intercept values of -0.6×10^{-5} and -1.2×10^{-5} m^2 s^2. For 12S, r^2 values were found to be 0.93 and 0.70 for $\overline{v'w'}$ and $\overline{u'v'}$, respectively, with slopes of 0.92 and 0.93 and intercept values of 2.8×10^{-5} and 0.5×10^{-5} m^2 s^2.
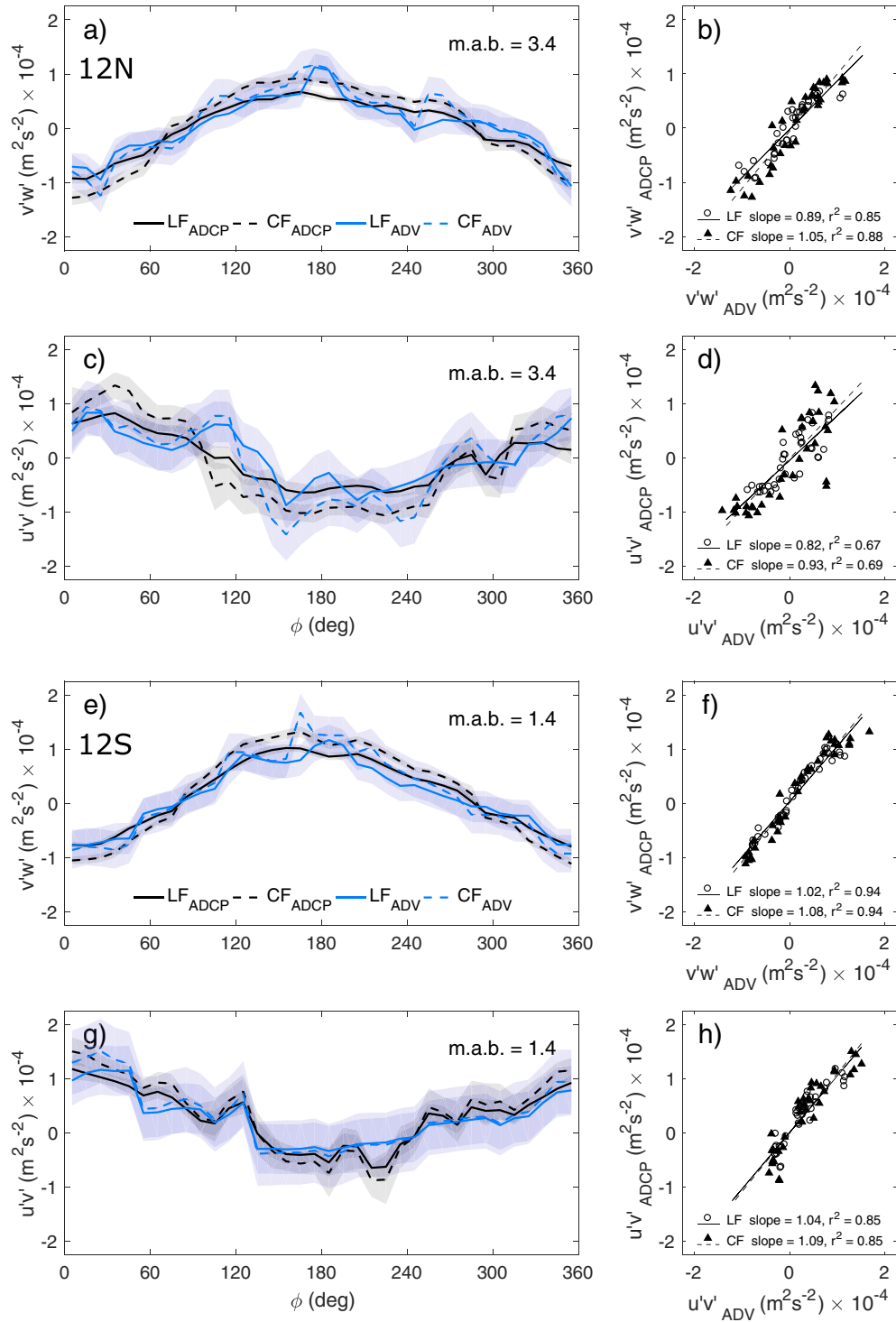
Fig. 8. Phase ensemble-average comparisons of ADV (blue lines) and ADCP (black lines) based on below-waveband stress estimates (LF, solid lines) and cospectra-fit method estimates (CF, dashed lines) for (**a**,**e**) vertical ($\overline{v'w'}$) and (**c**,**g**) lateral ($\overline{u'v'}$) turbulent stress estimates 3.4 and 1.4 m above the bed (m.a.b.) at 12N (**a**,**c**) and 12S (**e**,**g**), respectively. Right panels (**b**,**d**,**f**,**g**) show the corresponding linear regressions, slopes, and r^2 values between the ADCP and ADV for ensemble phase-averaged LF and CF stress estimates. Shaded regions (**a**,**c**,**e**,**g**) illustrate the 95% bootstrapped confidence intervals.

In general, the vertical stress comparisons (Fig. 8b,f) exhibit higher correlations than the lateral stress comparisons (Fig. 8d,h). This is consistent with results obtained in Section: *Uncertainty in stress measurements*, which show that lateral stress calculations are prone to higher uncertainty levels than the vertical stresses. Also, more scatter is observed for both the vertical and lateral stress
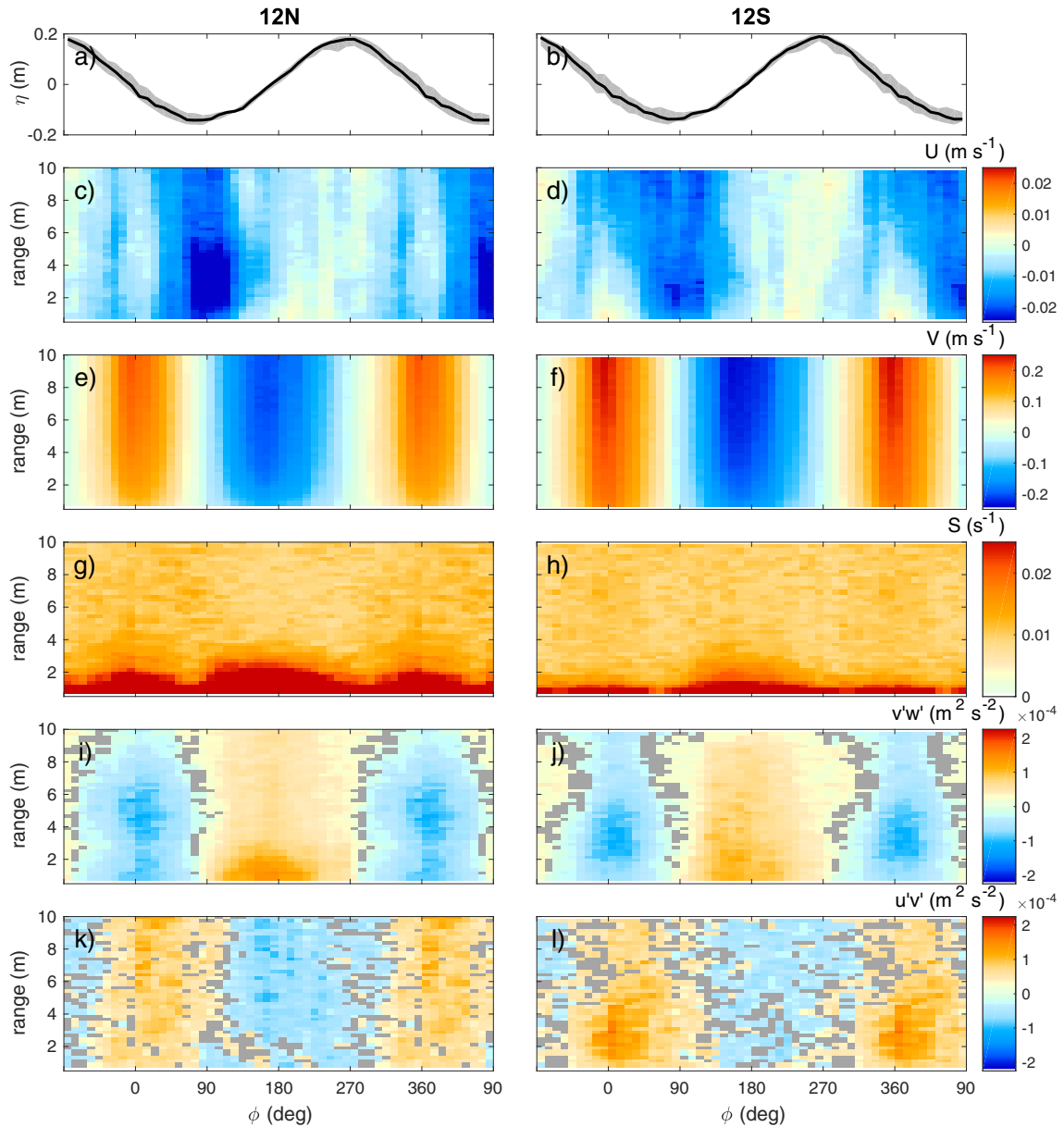
Fig. 9. Phase ensemble-averages of (**a,b**) sea surface height; (**c,d**) cross- and (**e,f**) alongshore velocities; (**g,h**) vertical shear magnitude; (**i,j**) vertical and (**k,l**) lateral below-waveband Reynolds stress estimates for (left) 12N and (right) 12S ADCPs. Red and blue tones indicate onshore and offshore flows in (**c**) and (**d**), respectively, and northward and southward flows in (**e**) and (**f**). Shaded regions in (**a**) and (**b**) show the 95% confidence intervals. Regions where the standard error exceeds the magnitude of the phase-averaged values are masked in gray in (**i**)–(**l**).

comparisons at 12N (Fig. 8b,d) relative to 12S (Fig. 8f,h). The higher scatter observed at 12N can be attributed to the separation distance between the ADCP and the ADV sensors. For 12N this separation distance was ~ 70 m, whereas for 12S the instruments were virtually collocated (*see* Fig. 1).

Figure 9 shows phase-averaged results for the sea surface height (η), and the vertical structure of the flow and of the below-waveband Reynolds stress estimates as a function of ADCP range cell for the 12N (Fig. 9a,c,e,g,i,k) and 12S (Fig. 9b,d,f,h,j,l) moorings. As described in Section: *Phase ensemble averaging*, the tidal phase is defined so that the depth-averaged alongshore flow

adheres to the shape of a cosine function ($\cos\phi$), with maximum northward and southward currents occurring around $\phi \approx 0°$ and $\phi \approx 180°$, respectively. Here, we have extended the phase (ϕ) axis by a half cycle to better illustrate variations around the maximum northward currents. Velocity and stress estimates are accepted as valid if their phase ensemble-averaged magnitudes exceed their corresponding $2\sigma/\sqrt{M}$ uncertainty levels, where σ is the standard deviation of the ensemble and M is the number of statistically independent samples. Estimates that do not meet this threshold are excluded and masked in gray in Fig. 9.

As shown in Fig. 9a,b,e,f, the sea surface height (η) and the alongshore velocities (V) are out of phase by about 45° throughout a tidal cycle. As noted by Arzeno et al. (2018), there was poor coherence (Coh^2 = 0.55) between the sea surface displacement and the velocity signal over the observational period; this accounts for the observed increase in scatter in η (Fig. 9a,b). The alongshore velocities at 12S were observed to be slightly higher (by about 10% at max velocities) than at 12N. Previous work at Makua has suggested that a large ($\sim$ 3 m) bathymetric step located approximately 25 m south of the mooring site could have resulted in local flow acceleration at 12S (Arzeno et al. 2018). For both sites, the cross-shore velocities (U) are about one order of magnitude smaller than the alongshore velocities, and exhibit a bottom intensified offshore flow (Fig. 9c,d) as the alongshore flow switches from northward to southward ($\phi \approx 90°$). Time-averaging over 50 cycles at the dominant M_2 period should eliminate most diurnal signals, though there may be some residual cross-shore flow associated with diurnal timescale thermally driven flow (e.g., Molina et al. 2014).

Consistent with theory for wall-bounded turbulent flows, the below-waveband vertical ($\overline{v'w'}$) Reynolds stress estimates (Fig. 9i,j) are in phase with the alongshore velocities (V), and exhibit maximum magnitudes near the bottom for southward flow at both sites, coincident with the region of maximum vertical shear $S = [(\partial V/\partial z) + (\partial U/\partial z)]^{1/2}$ (Fig. 9g,h). For northward flow, however, the maximum vertical stress magnitudes occur away from the bed, at a range of about 5 and 3 m.a.b. for 12N and 12S, respectively. Note that, for northward flow ($315° \lesssim \phi \lesssim 45°$), the magnitude of the vertical shear (S) does not exhibit a corresponding increase (Fig. 9g,h). This deviation suggests that vertical Reynolds stresses were modified by advection. We emphasize that these advective patterns are tidally coherent, and appear to have a characteristic vertical structure that varies as a function of tidal phase. It is therefore likely that the heterogeneous bathymetry in the vicinity of the ADCP locations (Fig. 1) is playing an important role in producing the observed structural features of the fluctuating flow. Consistent with the present findings, prior field studies conducted in reef morphologies with highly variable bathymetry have noted that advective acceleration can provide a non-negligible contribution to the local momentum budget (e.g., Rogers et al. 2015; Arzeno et al. 2018). This issue will be revisited in Section: *Discussion and conclusions*.

The lateral stress distributions at 12N exhibit a nearly uniform vertical structure across all phases, with a slight intensification in $\overline{u'v'}$ toward the surface for northward flow (Fig. 9k). On the other hand, results in Fig. 9l show an intensification in lateral stress ($\overline{u'v'}$) matching the location of maximum vertical stress for northward flow, and a relatively uniform vertical structure for southward flow at 12S. From Fig. 9i–l, it is apparent that the vertical and lateral stress components are comparable in magnitude. Furthermore, estimates of $\overline{u'v'}$ (Fig. 9i,j)

appear to be roughly in phase with $\overline{v'w'}$ and V, suggesting again that the lateral stress ($\overline{u'v'}$) could be related to the bottom-generated turbulence. This idea is explored further in the next section.

Model for lateral Reynolds stress

Following the turbulent viscosity hypothesis (Pope 2000), we relate the depth-averaged lateral Reynolds stresses to the cross-shore gradient of the mean alongshore velocity field

$$\widehat{u'v'} = -\nu_t \frac{\partial V}{\partial x} \tag{22}$$

where ν_t is a turbulent eddy viscosity, $\partial V/\partial x$ is the cross-shore gradient of the depth-averaged alongshore flow, and the hat ($\hat{}$) operator is used to represent a modeled lateral stress. To quantify the cross-shore gradient of the alongshore flow, we use depth- and spatially-averaged velocity measurements from three autonomous underwater vehicle (AUV) surveys conducted at the Makua forereef on 6–8 September 2013, as described by Amador et al. (2020). Briefly, AUV-based alongshore velocities are spatially-averaged using a cross-shore averaging length of 120 m. Because the AUV data covers roughly 60% of the tidal cycle, the depth-averaged alongshore flow is reconstructed for the full tidal cycle by fitting a sinusoid to the AUV data over a range of cross-shore locations. The cross-shore gradient of the alongshore flow ($\partial V/\partial x$) is then computed at the 12 m isobath (nominal depth at ADCP locations) from the reconstructed velocity field (Fig. 10a). Analysis by Amador et al. (2020) indicates that $\partial V/\partial x$ is caused by cross-shore variations in bottom drag.

From dimensional considerations, the eddy viscosity, ν_t, should be proportional to the product of a characteristic turbulent length scale λ_t and a turbulent velocity u_t. Here, we consider three simple models to represent the eddy viscosity in the form $\nu_t = \alpha u_t \lambda_t$:

$$\nu_{t1} = \alpha_1 \left|\overline{v'w'}\right|^{1/2} \lambda_{0u'v'} \ , \qquad \nu_{t2} = \alpha_2 \left|\frac{\partial V}{\partial x}\right| \lambda_{0u'v'}^2 \ ,$$
$$\nu_{t3} = \alpha_3 \left(C_D V^2\right)^{1/2} h \tag{23}$$

where α_j (j = 1, 2, 3) is a proportionality constant of order unity (in Fig. 10, $\alpha_j = 1$), C_D is a nondimensional drag coefficient for the depth-averaged alongshore flow (V), and h is the local water depth. The first formulation in Eq. (23) (solid blue line in Fig. 10b) assumes that lateral turbulence is modulated by bottom-driven turbulence, where the characteristic turbulent velocity is represented by the measured depth-averaged vertical stress, as $u_t \sim \left|\overline{v'w'}\right|^{1/2}$. The second formulation in Eq. (23) (dashed blue line in Fig. 10b) assumes that lateral transport is driven by lateral shear-driven turbulence using a conventional mixing length approach, $u_t \sim |\partial V/\partial x| \lambda_{0u'v'}$. The third formulation in Eq. (23) (dotted blue line in Fig. 10b) is analogous to ν_{t1} but recast in a parametric form that makes
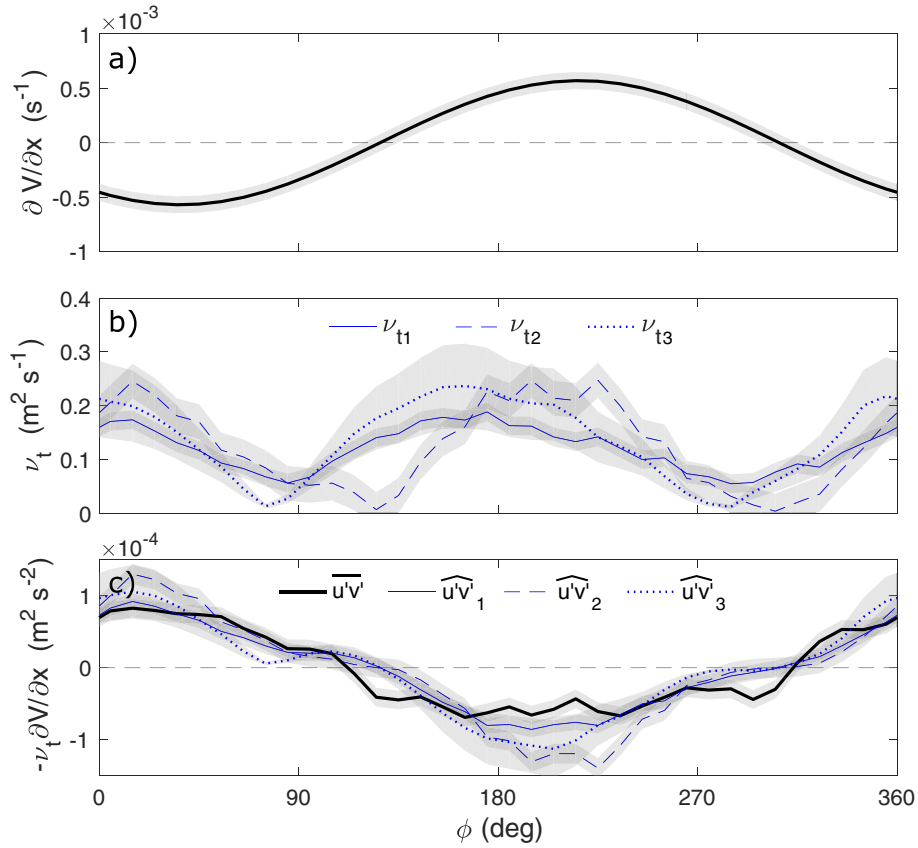
Fig. 10. (**a**) Cross-shore gradient of the depth-averaged alongshore flow at the 12-m isobath from AUV spatial velocity measurements; (**b**) three eddy viscosity models in Eq. (23); and (**c**) corresponding lateral stress models (Eq. 22) (blue lines) along with the phase- and depth-averaged lateral Reynolds stress estimates for the 12N ADCP (thick black line). Shaded regions indicate the 95% confidence intervals calculated via bootstrapping and error propagation, as described by Emery and Thomson (1997).

use of readily available quantities. Similar to ν_{t1}, the third model (ν_{t3}) assumes that bottom turbulence ($u_t \sim u_* = \sqrt{C_D V^2}$) dominates the transport of lateral turbulent fluxes, where u_* is a friction velocity that characterizes the shear at the bed. Consistent with our observations (*see* Section: *Turbulence length scales*), ν_{t3} postulates that the turbulent length (λ_t) scales with the local water depth (h). This is in contrast to both ν_{t1} and ν_{t2}, for which the turbulent length scale is given by $\lambda_t \sim \lambda_{0u'v'}$, a measured quantity determined from the lateral stress cospectra (*see* Fig. 7b). Note also that ν_{t1} and ν_{t3} are roughly in phase with the alongshore flow, whereas ν_{t2} has a slight lag as it varies more closely with $|\partial V/\partial x|$.

The resulting eddy viscosity models for ADCP 12N are plotted in Fig. 10b as a function of tidal phase. Figure 10c shows a comparison between the modeled $\left(\widehat{u'v'}\right)_j$ (blue lines) and measured ($\overline{u'v'}$) lateral stress estimates for ADCP 12N (thick black line). The modeled lateral stresses are obtained by substituting Eq. (23) in Eq. (22), with order one constants chosen as $\alpha_1 = \alpha_2 = \alpha_3 = 1$. Analysis by Amador et al. (2020) gives a drag coefficient $C_D = 0.0081 \pm 0.0025$ in the vicinity of ADCP

locations, which is used here. The water depths at 12N and 12S are 13.2 and 11.7 m, respectively, as shown in Table 1.

From Fig. 10(c), it is apparent that the shapes of the predicted lateral stress profiles agree well the observational data, with r^2 values of 0.89, 0.81, and 0.84 for $\widehat{u'v'}_1$, $\widehat{u'v'}_2$, and $\widehat{u'v'}_3$, respectively. Similar results were obtained for ADCP 12S (not shown), with slightly higher r^2 values in all cases: 0.92, 0.85, and 0.89 for $\widehat{u'v'}_1$, $\widehat{u'v'}_2$, and $\widehat{u'v'}_3$, respectively. A statistical comparison (Diedenhofen and Musch 2015) of the r^2 values associated with $\widehat{u'v'}_1$ and $\widehat{u'v'}_2$ showed the relationships to be significantly different ($p < 0.001$). No statistically significant differences were found between the r^2 values corresponding to $\widehat{u'v'}_1$ and $\widehat{u'v'}_3$ ($p > 0.05$). The similarity among the correlations is not surprising, given that both $\partial V/\partial x$ and $\overline{v'w'}$ are largely determined by V. The difference between $\widehat{u'v'}_2$ and the other quantities ($\overline{u'v'}$, $\widehat{u'v'}_1$, $\widehat{u'v'}_3$) is primarily associated with the slight phase shift in $\partial V/\partial x$ (note that $\widehat{u'v'}_2$ is more heavily weighted toward $\partial V/\partial x$). Overall, these results suggest that the strongest association is between

$\overline{u'v'}$ and $\widehat{u'v'}_1$ which applies ν_{t1}, but we note that the simpler model, ν_{t3}, which uses readily available quantities, also works well.

Discussion and conclusions

This represents one of the first attempts at quantifying the vertical structure of the lateral Reynolds stresses ($\overline{u'v'}$) in the coastal ocean. In this study, we have assessed the use of an ADCP for measurements of $\overline{u'v'}$ in the presence of surface gravity waves by modifying existing wave-turbulence decomposition techniques (Kirincich et al. 2010) to enable robust estimates of the below-waveband stresses. Although instantaneous $\overline{u'v'}$ estimates suffer from a low signal-to-noise ratio, tidal phase averaging reduces the noise sufficiently, allowing for a clear analysis of the lateral Reynolds stresses over the tidal cycle.

Assessment of the method via comparisons with independent ADV-based stress estimates at the 12N and 12S moorings showed good quantitative agreement over the tidal cycle (Fig. 8), confirming that ADCPs can effectively resolve lateral turbulent fluxes and isolate them from wave-induced errors. Furthermore, results in Fig. 5 indicate that most of the turbulent covariance is explained by low-frequency (below the waveband) turbulent motions. Therefore, below-waveband estimates of $\overline{v'w'}$, $k_{0v'w'}$, and of $\overline{u'v'}$, $k_{0u'v'}$, determined empirically from the phase-averaged cospectra, can be interpreted and assessed with confidence as reasonably accurate representations of the actual phase-averaged values. Estimates of $\overline{u'v'}$ are roughly in phase with $\overline{v'w'}$ and V, and appear to have a fairly uniform vertical structure with deviations that correlate with the vertical stresses (Fig. 9i–l) and that suggest an influence of advection. Note, however, that these estimates represent local values obtained by point sensors and are not necessarily representative of reef-scale averages due to the highly irregular and complex reef topography (Trowbridge and Lentz 2018). Below, we discuss limitations in the method along with implications of the results.

Method limitations

The applicability of the proposed method for lateral stress measurements is principally limited by the geometric length scale imposed by beam separation (Section: *Vertical and lateral stress covariances from along-beam velocity fluctuations*), the wave cutoff frequency (Section: *Wave-turbulence decomposition*), the instrument alignment relative to the flow (Section: *Alignment errors*), and by measurement uncertainty (Section: *Uncertainty in stress measurements*). Application of the method also requires careful consideration of potential non-turbulent processes occurring at the turbulence time-scales. These can produce concurrent horizontal velocity fluctuations and introduce errors into the lateral stress estimates. In this study, turbulent fluctuations were found to be the dominant source of velocity covariances at frequencies below the waveband.

Consideration of the pressure spectra indicates that infragravity motions accounted for less than 2% of total observed covariance (Section: *Screening criteria*) and fluctuations due to internal waves were highly unlikely since stratification was virtually non-existent during the observational period (Section: *Field deployment*).

For this study, the horizontal length scales of the dominant stress-carrying turbulent motions always exceeded the beam separation scale and often surpassed the flow depth. The results of this study showed that the minimum resolved lateral turbulent length scales were generally greater than the separation scale of the adjacent beam pairs (over 70% of the quality-controlled bursts). In other words, the smallest resolvable turbulent motions were mostly constrained by the wave cutoff rather than the beam separation scale. While turbulence is undoubtedly present at these unresolved scales, the variance preserving cospectra (Fig. 5c,d) and ogive curves (Fig. 5g,h) indicate that these residual small-scale turbulent motions do not contribute significantly to the overall lateral stress. The method was therefore capable of capturing the majority of the turbulent stress at frequencies below those corresponding to the cutoff scales.

As for the uncertainty errors, it was found that lateral stress uncertainties were higher than the stress estimates for a significant fraction of the bursts, and about 2.8 times higher than the vertical stress uncertainties (Fig. 4), likely due to the ADCP geometry. The limited accuracy of individual lateral stress measurements renders them unreliable for practical applications. However, tidal phase ensemble-averaging substantially reduced the lateral stress uncertainties, resulting in standard errors well below the estimated Reynolds stresses for the majority of the ensembles (Fig. 9k,l). We note that phase averaging requires a periodic flow field and may not be appropriate in many scenarios. Ensemble-averaging by tidal phase could also bias stress estimates toward periods of stronger tides since the Reynolds stresses are a non-linear quantity. Our analysis shows that these effects are minimal, however, for our observations. Here, both the orientation of the ADCPs (12N, 12S) relative to the alongshore flow (Table 1) and the hydrodynamic conditions were particularly well suited for testing our technique and for elucidating the tidally-varying vertical structure of the lateral Reynolds stress.

The spectral wave-turbulence decomposition technique described in this study is also limited by the properties of the wave field because the unsteady advection of turbulence by wave orbital velocities can alter the shape of the observed cospectrum. To ensure viable stress estimates and limit the kinematic effects of wave orbital motion, we restricted our observations to instances when $\sigma_w/|v_c| < 2$ and $\sigma_w k_0/\omega_w < 0.5$ (Fig. 6). Analysis by Rosman and Gerbi (2017) predicts that under such conditions, at least 80% of the turbulent covariance is expected to reside at frequencies below the wave peak. However, it is important to bear in mind that these screening criteria effectively bias our observations toward times of more

energetic flows and weaker waves (Kirincich et al. 2010; Kirincich 2013). As a result, it is unknown whether the influence of energetic surface waves affects the magnitude and vertical structure of the observed lateral stresses, though wave forcing is expected to enhance the near-bed vertical stresses and increase bottom drag (Lentz et al. 2018; Scully et al. 2018).

Implications of the results

Results presented in Fig. 9i–l illustrate the vertical structure of the phase ensemble-averaged turbulent Reynolds stresses resulting from well-mixed (unstratified), tidally-driven flow over rough coral reef bathymetry for weak swell conditions ($H_s \lesssim 0.6$ m) (Fig. 2). Observations of the vertical stress (Fig. 9i, j) show that $\overline{v'w'}$ does not coincide with regions of vertical shear (S) over a significant fraction of the tidal cycle. This is indicative of local imbalances between production and dissipation of turbulent kinetic energy, and suggests non-negligible contributions from advective transport. Indeed, Arzeno et al. (2018) has reported that advective acceleration plays an important role in the local momentum budget at Makua, and is necessary for budget closure at 12S. Recent studies have shown that irregular roughness induces spatial gradients in the Reynolds stresses and promotes the production of turbulent kinetic energy in preferential regions, which requires the presence of secondary advective velocities (Mejia-Alvarez and Christensen 2013; Barros and Christensen 2014; Anderson et al. 2015). Notably, Rogers et al. (2015) suggested that a similar mechanism was likely responsible for the formation of secondary circulations over spur and groove morphology. Thus, it is likely that the complex, multi-scaled bathymetric nature of spur and groove formations results in Reynolds stress distributions that are highly variable in space, and lead to advective transport by virtue of secondary flows.

For the Makua site, the cross-shore structure of the mean alongshore velocity and the associated lateral shear are determined by cross-shore variations in bottom drag (Amador et al. 2020). Work by Vermaas et al. (2011) and Willingham et al. (2014) indicate that lateral variations in bottom roughness and the resultant wall stress distribution induce a corresponding lateral shear, which facilitates a lateral momentum exchange via $\overline{u'v'}$. This is consistent with results in Fig. 9k,l, which show a detectable lateral stress ($\overline{u'v'}$) signal that is sustained by a cross-shore gradient in the alongshore velocity (Fig. 10a) and that extends throughout the water column.

Using the estimated turbulent quantities ($\overline{v'w'}$, $\overline{u'v'}$, $\lambda_{0u'v'}$), the lateral gradient of the depth-averaged alongshore velocity ($\partial V/\partial x$), and assuming a turbulent-viscosity framework (22), we tested three simple eddy viscosity (ν_t) formulations (23) to help elucidate the underlying mechanisms responsible for generating the observed lateral stresses. The first two formulations (ν_{t1}, ν_{t2}) were based on estimated turbulent quantities, whereas the third one (ν_{t3}) was based on a solely parametric

formulation. Although all three models satisfactorily reproduce the observed depth-averaged lateral stresses (Fig. 10c), the statistical results (Section: *Model for lateral Reynolds stress*) indicate that the proposed bottom generated turbulence models ($\widehat{u'v'}_1$, $\widehat{u'v'}_3$) are marginally better than the lateral mixing length model ($\widehat{u'v'}_2$) at capturing the phase variations in the estimated lateral stresses. The idea that bottom-driven turbulence modulates $\overline{u'v'}$ is also consistent with the experimental results in Fig. 7, which show that the stress-carrying turbulent horizontal length scales are on the order of the local water depth $O(10 \text{ m})$ and not on the scale of the coastal boundary layer $O(1000 \text{ m})$; thus, implying a potential connection between the bottom-driven turbulence and horizontal turbulence. Further research is required to examine more closely the links between $\overline{v'w'}$, $\overline{u'v'}$, and ν_t in flow over rough topography.

Finally, with regard to cross-shelf transport, the role of the lateral Reynolds stresses can be compared to cross-shore advective transport via a Péclet number

$$Pe = \frac{UL_x}{\nu_t} \sim 10^2 \tag{24}$$

where $L_x \sim 10^3$ m is the cross-shore distance from the shoreline to the ADCPs, and $U \sim 10^{-2}$ m s^{-1} and $\nu_t \sim 10^{-1}$ m^2 s^{-1} from our observations (*see* Figs. 9c,d and 10b). From Eq. (24) we can conclude that, at Makua, the lateral transport by turbulent mixing is negligible in comparison to the lateral advective transport over the course of the tidal cycle. However, it is worth noting that, at Makua, the lateral turbulent diffusivity is in phase with the alongshore flow, and usually out of phase with the cross-shore tidal velocities; hence, lateral turbulent diffusion may dominate over cross-shore advective transport when the tidal cross-shore velocities are at their minimum. Moreover, turbulent diffusion is an irreversible mixing process, as opposed to advective transport, which is a dispersive and reversible process. Furthermore, if we allow the eddy viscosity to scale as ν_{t3} in Eq. (23) (assuming $\lambda_{0u'v'} \sim h$), then we may rewrite Eq. (24) as

$$Pe_3 = \frac{U}{\alpha_3 C_D^{1/2} V \beta}$$

where $\beta = h/L_x$ is the cross-shore seafloor slope. For the observed conditions at Makua ($\alpha_3 = 1$, $C_D \sim 0.01$, $\beta \sim 0.04$, $V \sim 10^{-1}$ m s^{-1}), this gives $Pe_3 = 25$. This suggests that lateral transport by turbulent mixing could be relevant to an important subset of coral reef shelves: those with sufficiently steep slopes and rough bottoms, which are typical features of many fore-reefs around the world (e.g., Lewis and Hutchinson 2001; Rosman and Hench 2011; Quataert et al. 2015).

Data availability statement

The data used in this research are available online as part of the UCSD Library Digital Collections with the identifiers

https://doi.org/10.6075/J09G5K1F   and   https://doi.org/10.
6075/J09P3042.

References

Amador, A., I. B. Arzeno, S. N. Giddings, M. Merrifield, and G. Pawlak. 2020. Cross-shore structure of tidally driven along-shore flow over rough bathymetry. J. Geophys. Res. Oceans **125**: e2020JC016264. doi:10.1029/2020JC016264

Anderson, W., J. M. Barros, K. T. Christensen, and A. Awasthi. 2015. Numerical and experimental study of mechanisms responsible for turbulent secondary flows in boundary layer flows over spanwise heterogeneous roughness. J. Fluid Mech. **768**: 316–347. doi:10.1017/jfm.2015.91

Arzeno, I. B., A. Collignon, M. Merrifield, S. N. Giddings, and G. Pawlak. 2018. An alongshore momentum budget over a fringing tropical fore-reef. J. Geophys. Res. Oceans **123**: 7839–7855. doi:10.1029/2018JC014238

Atkinson, M., J. Falter, and C. J. Hearn. 2001. Nutrient dynamics in the biosphere 2 coral reef mesocosm: Water velocity controls NH4 and PO4 uptake. Coral Reefs **20**: 341–346. doi:10.1007/s00338-001-0184-7

Baird, M., and M. Atkinson. 1997. Measurement and prediction of mass transfer to experimental coral reef communities. Limnol. Oceanogr. **42**: 1685–1693. doi:10.4319/lo.1997.42.8.1685

Barros, J. M., and K. T. Christensen. 2014. Observations of turbulent secondary flows in a rough-wall boundary layer. J. Fluid Mech. **748**: R1. doi:10.1017/jfm.2014.218

Bian, C., Z. Liu, Y. Huang, L. Zhao, and W. Jiang. 2018. On estimating turbulent Reynolds stress in wavy aquatic environment. J. Geophys. Res. Oceans **123**: 3060–3071. doi:10.1002/2017JC013230

Bricker, J. D., and S. G. Monismith. 2007. Spectral wave–turbulence decomposition. J. Atmos. Oceanic Tech. **24**: 1479–1487. doi:10.1175/JTECH2066.1

Brink, K. H. 2016. Cross-shelf exchange. Ann. Rev. Mar. Sci. **8**: 59–78. doi:10.1146/annurev-marine-010814-015717

Burchard, H. 2002. Applied turbulence modelling in marine waters, v. **100**. Springer Science & Business Media. doi:10.1007/3-540-45419-5

Burchard, H., and and other. 2008. Observational and numerical modeling methods for quantifying coastal ocean turbulence and mixing. Prog. Oceanogr. **76**: 399–442. doi:10.1016/j.pocean.2007.09.005

Davis, K. A., G. Pawlak, and S. G. Monismith. 2021. Turbulence and coral reefs. Ann. Rev. Mar. Sci. **13**: 343–373. doi:10.1146/annurev-marine-042120-071823

Dewey, R. and Stringer, S. (2007) Reynolds stresses and turbulent kinetic energy estimates from various ADCP beam configurations: Theory, unpublished. Available from https://www.researchgate.net/publication/280100811_Reynolds_Stresses_and_Turbulent_Kinetic_Energy_Estimates_from_Various_ADCP_Beam_Configurations_Theory.

Diedenhofen, B., and J. Musch. 2015. Cocor: A comprehensive solution for the statistical comparison of correlations. PloS one **10**: e0121945. doi:10.1371/journal.pone.0121945

Emery, W., and R. Thomson. 1997. Data analysis methods in physical oceanography. Pergamon.

Feddersen, F., and A. Williams. 2007. Direct estimation of the Reynolds stress vertical structure in the nearshore. J. Atmos. Oceanic Tech. **24**: 102–116. doi:10.1175/JTECH1953.1

Gerbi, G. P., J. H. Trowbridge, J. B. Edson, A. J. Plueddemann, E. A. Terray, and J. J. Fredericks. 2008. Measurements of momentum and heat transfer across the air–sea interface. J. Phys. Oceanogr. **38**: 1054–1072. doi:10.1175/2007JPO3739.1

Gross, T. F., and A. R. Nowell. 1985. Spectral scaling in a tidal boundary layer. J. Phys. Oceanogr. **15**: 496–508. doi:10.1175/1520-0485(1985)015<0496:SSIATB>2.0.CO;2

Jones, G., G. Almany, G. Russ, P. Sale, R. Steneck, M. Van Oppen, and B. Willis. 2009. Larval retention and connectivity among populations of corals and reef fishes: History, advances and challenges. Coral Reefs **28**: 307–325. doi:10.1007/s00338-009-0469-9

Kaimal, J. C., J. Wyngaard, Y. Izumi, and O. Coté. 1972. Spectral characteristics of surface-layer turbulence. Q. J. Roy. Meteorol. Soc. **98**: 563–589.

Kirincich, A. R. 2013. Long-term observations of turbulent Reynolds stresses over the inner continental shelf. J. Phys. Oceanogr. **43**: 2752–2771. doi:10.1175/JPO-D-12-0153.1

Kirincich, A. R., S. J. Lentz, and G. P. Gerbi. 2010. Calculating Reynolds stresses from ADCP measurements in the presence of surface gravity waves using the cospectra-fit method. J. Atmos. Oceanic Tech. **27**: 889–907. doi:10.1175/2009JTECHO682.1

Kirincich, A. R., and J. H. Rosman. 2011. A comparison of methods for estimating Reynolds stress from ADCP measurements in wavy environments. J. Atmos. Oceanic Tech. **28**: 1539–1553. doi:10.1175/JTECH-D-11-00001.1

Lentz, S. J., J. H. Churchill, and K. A. Davis. 2018. Coral reef drag coefficients–surface gravity wave enhancement. J. Phys. Oceanogr. **48**: 1555–1566. doi:10.1175/JPO-D-17-0231.1

Lewis, A., and S. Hutchinson. 2001. Great barrier reef depth and elevation model: GBRDEM. CRC Reef Research Centre.

Lohrmann, A., B. Hackett, and L. P. Røed. 1990. High resolution measurements of turbulence, velocity and stress using a pulse-to-pulse coherent sonar. J. Atmos. Oceanic Tech. **7**: 19–37. doi:10.1175/1520-0426(1990)007<0019:HRMOTV>2.0.CO;2

Lu, Y., and R. G. Lueck. 1999. Using a broadband ADCP in a tidal channel. Part II: Turbulence. J. Atmos. Oceanic Tech. **16**: 1568–1579. doi:10.1175/1520-0426(1999)016<1568:UABAIA>2.0.CO;2

Lumley, J., and E. Terray. 1983. Kinematics of turbulence convected by a random wave field. J. Phys. Oceanogr. **13**: 2000–2007. doi:10.1175/1520-0485(1983)013<2000:KOTCBA>2.0.CO;2

Mejia-Alvarez, R., and K. T. Christensen. 2013. Wall-parallel stereo particle-image velocimetry measurements in the

roughness sublayer of turbulent flow overlying highly irregular roughness. Phys. Fluids **25**: 115109. doi:10.1063/1.4832377

Molina, L., G. Pawlak, J. Wells, S. Monismith, and M. A. Merrifield. 2014. Diurnal cross-shore thermal exchange on a tropical forereef. J. Geophys. Res. Oceans **119**: 6101–6120. doi:10.1002/2013JC009621

Monismith, S. G. 2007. Hydrodynamics of coral reefs. Annu. Rev. Fluid Mech. **39**: 37–55. doi:10.1146/annurev.fluid.38.050304.092125

Nezu, I., and H. Nakagawa. 1993. Turbulence in open-channel flows. Routledge.

Nidzieko, N. J., D. A. Fong, and J. L. Hench. 2006. Comparison of Reynolds stress estimates derived from standard and fast-ping ADCPs. J. Atmos. Oceanic Tech. **23**: 854–861. doi:10.1175/JTECH1885.1

Pope, S. B. 2000. Turbulent flows. Cambridge Univ. Press.

Quataert, E., C. Storlazzi, A. Van Rooijen, O. Cheriton, and A. Van Dongeren. 2015. The influence of coral reefs and climate change on wave-driven flooding of tropical coastlines. Geophys. Res. Lett. **42**: 6407–6415. doi:10.1002/2015GL064861

Rogers, J. S., S. G. Monismith, R. B. Dunbar, and D. Koweek. 2015. Field observations of wave-driven circulation over spur and groove formations on a coral reef. J. Geophys. Res. Oceans **120**: 145–160. doi:10.1002/2014JC010464

Rosman, J. H., and G. P. Gerbi. 2017. Interpreting fixed-location observations of turbulence advected by waves: Insights from spectral models. J. Phys. Oceanogr. **47**: 909–931. doi:10.1175/JPO-D-15-0249.1

Rosman, J. H., and J. L. Hench. 2011. A framework for understanding drag parameterizations for coral reefs. J. Geophys. Res. Oceans **116**: C08025. doi:10.1029/2010JC006892

Rosman, J. H., J. L. Hench, J. R. Koseff, and S. G. Monismith. 2008. Extracting Reynolds stresses from acoustic Doppler current profiler measurements in wave-dominated environments. J. Atmos. Oceanic Tech. **25**: 286–306. doi:10.1175/2007JTECHO525.1

Scully, M. E., J. H. Trowbridge, C. R. Sherwood, K. R. Jones, and P. Traykovski. 2018. Direct measurements of mean Reynolds stress and ripple roughness in the presence of energetic forcing by surface waves. J. Geophys. Res. Oceans **123**: 2494–2512. doi:10.1002/2017JC013252

Sevadjian, J. C., M. McManus, and G. Pawlak. 2010. Effects of physical structure and processes on thin zooplankton layers in Mamala Bay, Hawaii. Marine Ecol. Prog. Ser. **409**: 95–106. doi:10.3354/meps08614

Shaw, W. J., and J. H. Trowbridge. 2001. The direct estimation of near-bottom turbulent fluxes in the presence of energetic wave motions. J. Atmos. Oceanic Tech. **18**: 1540–1557. doi:10.1175/1520-0426(2001)018<1540:TDEONB>2.0.CO;2

Smalley, R., S. Leonardi, R. Antonia, L. Djenidi, and P. Orlandi. 2002. Reynolds stress anisotropy of turbulent rough wall layers. Exp. Fluids **33**: 31–37. doi:10.1007/s00348-002-0466-z

Stacey, M. T., S. G. Monismith, and J. R. Burau. 1999a. Measurements of Reynolds stress profiles in unstratified tidal flow. J. Geophys. Res. Oceans **104**: 10933–10949.

Stacey, M. T., S. G. Monismith, and J. R. Burau. 1999b. Observations of turbulence in a partially stratified estuary. J. Phys. Oceanogr. **29**: 1950–1970.

Trowbridge, J. 1998. On a technique for measurement of turbulent shear stress in the presence of surface waves. J. Atmos. Oceanic Tech. **15**: 290–298. doi:10.1175/1520-0426(1998)015<0290:OATFMO>2.0.CO;2

Trowbridge, J., and S. Elgar. 2001. Turbulence measurements in the surf zone. J. Phys. Oceanogr. **31**: 2403–2417. doi:10.1175/1520-0485(2001)031<2403:TMITSZ>2.0.CO;2

Trowbridge, J. H., and S. J. Lentz. 2018. The bottom boundary layer. Ann. Rev. Mar. Sci. **10**: 397–420. doi:10.1146/annurev-marine-121916-063351

Trowbridge, J., M. Scully, and C. R. Sherwood. 2018. The cospectrum of stress-carrying turbulence in the presence of surface gravity waves. J. Phys. Oceanogr. **48**: 29–44. doi:10.1175/JPO-D-17-0016.1

Vermaas, D., W. Uijttewaal, and A. Hoitink. 2011. Lateral transfer of streamwise momentum caused by a roughness transition across a shallow channel. Water Resour. Res. **47**: W02530. doi:10.1029/2010WR010138

Whipple, A. C., R. A. Luettich, and H. E. Seim. 2006. Measurements of Reynolds stress in a wind-driven lagoonal estuary. Ocean Dyn. **56**: 169–185. doi:10.1007/s10236-005-0038-x

Williams, E., and J. H. Simpson. 2004. Uncertainties in estimates of Reynolds stress and TKE production rate using the ADCP variance method. J. Atmos. Oceanic Tech. **21**: 347–357. doi:10.1175/1520-0426(2004)021<0347:UIEORS>2.0.CO;2

Willingham, D., W. Anderson, K. T. Christensen, and J. M. Barros. 2014. Turbulent boundary layer flow over transverse aerodynamic roughness transitions: Induced mixing and flow characterization. Phys. Fluids **26**: 025111. doi:10.1063/1.4864105